Article

SARS-CoV-2 mRNA vaccines sensitize tumours to immune checkpoint blockade

https://doi.org/10.1038/s41586-025-09655-y

Received: 6 November 2024

Accepted: 19 September 2025

Published online: 22 October 2025

Open access

Check for updates

Adam J. Grippin[1,29]✉, Christiano Marconi[2,29], Sage Copling[3,29], Nan Li[1,29], Chen Braun[1], Cole Woody[1], Elliana Young[4], Priti Gupta[1], Min Wang[1], Annette Wu[1], Seong Dong Jeong[5,6], Dhruvkumar Soni[2], Frances Weidert[2], Chao Xie[2], Eden Goldenberg[2], Andrew Kim[3], Chong Zhao[2], Anna DeVries[2], Paul Castillo[2,7], Rishabh Lohray[8], Michael K. Rooney[1], Benjamin R. Schrank[1], Yifan Wang[1], Yifan Ma[1], Enoch Chang[1], Ramez Kouzy[1], Kyle Dyson[9], Jordan Jafarnia[3], Nina Nariman[3], Gregory Gladish[10], Jacob New[11], Ada Argueta[1], Diana Amaya[1], Nagheme Thomas[2], Andria Doty[2], Joe Chen[1], Nikhil Copling[12], Gabriel Alatrash[1], Julie Simon[13], Alicia Bea Davies[13], William Dennis[1], Richard Liang[1], Jeff Lewis[14], Xiong Wei[14], Waree Rinsurongkawong[14], Ara A. Vaporciyan[15], Andrew Johns[16], D3CODE Team[17]*, Jack Lee[18], Ji-Hyun Lee[19], Ryan Sun[18], Padmanee Sharma[16,20,21], Hai Tran[14], Jianjun Zhang[14], Don L. Gibbons[14], Jennifer Wargo[13], Betty Y. S. Kim[5,6], John V. Heymach[14], Hector R. Mendez-Gomez[2], Wen Jiang[1], Elias J. Sayour[2,7,30]✉ & Steven H. Lin[1,30]✉

Immune checkpoint inhibitors (ICIs) extend survival in many patients with cancer but are ineffective in patients without pre-existing immunity[1–9]. Although personalized mRNA cancer vaccines sensitize tumours to ICIs by directing immune attacks against preselected antigens, personalized vaccines are limited by complex and time-intensive manufacturing processes[10–14]. Here we show that mRNA vaccines targeting SARS-CoV-2 also sensitize tumours to ICIs. In preclinical models, SARS-CoV-2 mRNA vaccines led to a substantial increase in type I interferon, enabling innate immune cells to prime $CD8^+$ T cells that target tumour-associated antigens. Concomitant ICI treatment is required for maximal efficacy in immunologically cold tumours, which respond by increasing PD-L1 expression. Similar correlates of vaccination response are found in humans, including increases in type I interferon, myeloid–lymphoid activation in healthy volunteers and PD-L1 expression on tumours. Moreover, receipt of SARS-CoV-2 mRNA vaccines within 100 days of initiating ICI is associated with significantly improved median and three-year overall survival in multiple large retrospective cohorts. This benefit is similar among patients with immunologically cold tumours. Together, these results demonstrate that clinically available mRNA vaccines targeting non-tumour-related antigens are potent immune modulators capable of sensitizing tumours to ICIs.

Although ICIs substantially improve survival in some patients, most patients do not benefit from these therapies[1–9]. These poor responses are attributed to immunosuppressive tumour microenvironments (TMEs) characterized by tolerogenic dendritic cells (DCs), myeloid suppressor cells and regulatory T cells, and may be predicted in some histologies by low intratumoural PD-L1 before immunotherapy initiation. However, there are currently no clinically available methods to improve responses to ICI by modifying the TME. We recently reported that systemic administration of highly immunogenic mRNA nanoparticles induces a viraemia-like cytokine/chemokine response that resets the systemic and intratumoural immune milieu, sensitizing resistant tumours to ICIs[10–12,14]. Although the personalized mRNA vaccines that we and others are developing remain in clinical evaluation (NCT04573140)[12], COVID-19 mRNA vaccines also induce robust stimulation of cytokine secretion[15], and there are now multiple case reports of patients whose tumours spontaneously resolved after COVID-19 mRNA vaccines[16,17]. However, the impact of COVID-19 mRNA vaccines on immune therapy is unknown.

Here we report that the innate immune response to SARS-CoV-2 spike mRNA vaccination resets the cancer immunotherapy cycle and primes adaptive immunity for synergy with ICIs. We found that receipt of a SARS-CoV-2 mRNA vaccine within 100 days of ICI initiation was associated with substantial improvements in overall survival (OS) in patients with non-small cell lung cancer (NSCLC) and melanoma. In preclinical models, we found that this effect required a surge in type-I interferon (IFN) that enhanced antigen-presenting cell (APC) priming of T cells in lymphoid organs. Although tumour cells subvert these primed responses by increasing PD-L1 expression, co-administration of ICIs sustains T cell responses and elicits epitope spreading against tumour-associated antigens. We revealed analogous response correlates for humans receiving COVID-19 mRNA vaccines, including heightened IFNα production, innate/adaptive immune activation and

A list of affiliations appears at the end of the paper. *A list of authors and their affiliations appears at the end of the paper. ✉e-mail: agrippin@mdanderson.org; elias.sayour@neurosurgery.ufl.edu; shlin@mdanderson.org

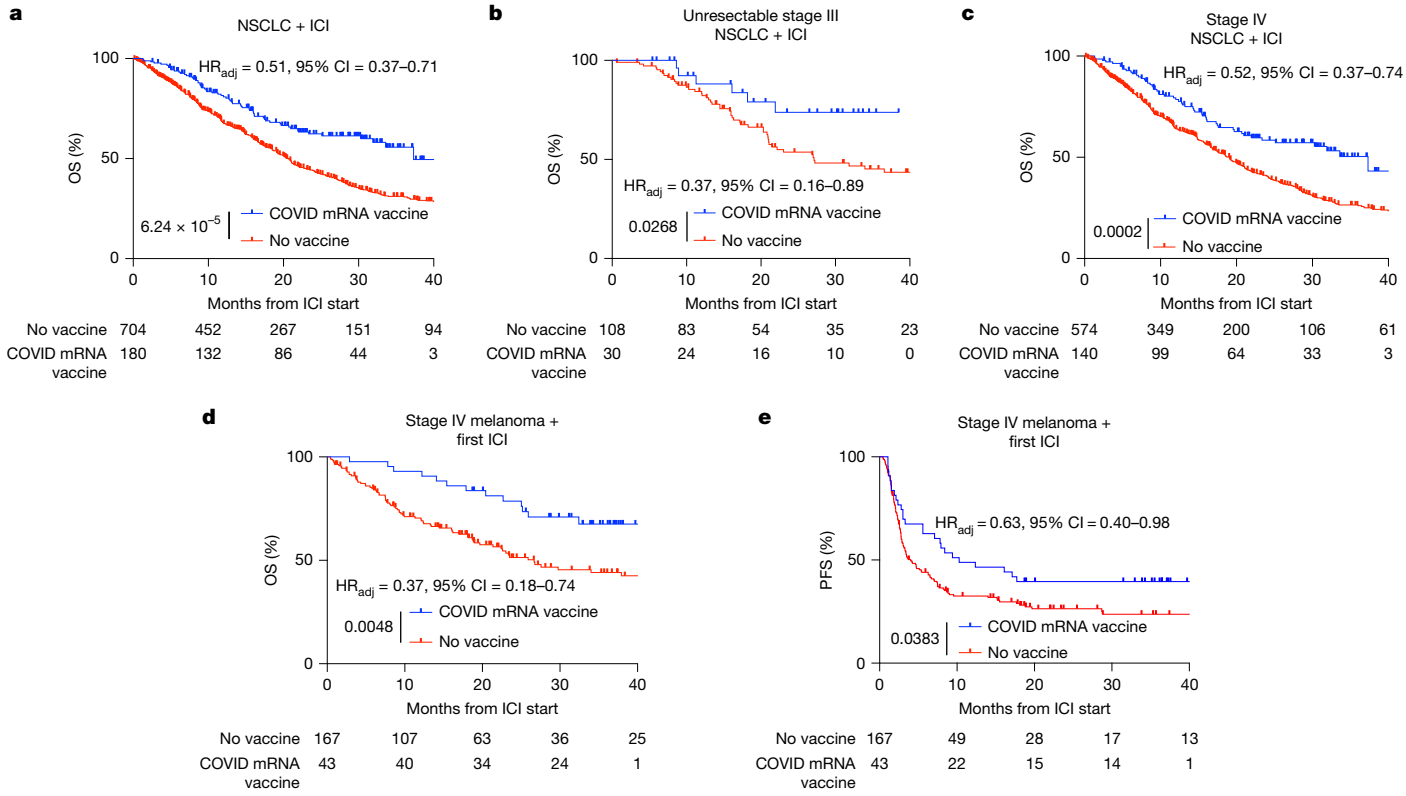

Fig. 1 | COVID-19 mRNA vaccines are associated with improved survival in patients with NSCLC or metastatic melanoma receiving immunotherapy. **a**–**e**, Survival for patients with NSCLC (**a**–**c**) or metastatic melanoma (**d**,**e**) treated with ICI who received a COVID-19 mRNA vaccine within 100 days of initiating ICI or did not receive a COVID-19 mRNA vaccine. Survival is shown for all patients with NSCLC (**a**), patients with unresectable stage III NSCLC (**b**), patients with stage IV NSCLC (**c**) and patients with metastatic melanoma (**d** and **e**). *P* values and HR$_{adj}$ were calculated using two-sided Cox proportional hazards regression (Supplementary Tables 3, 5, 7, 9 and 11), including all variables that were significantly associated with survival on univariable analysis (Supplementary Tables 2, 4, 6, 8 and 10). The number of patients at risk at each timepoint is indicated below each graph.

increases in tumour PD-L1 expression. Together, our results demonstrate that clinically available mRNA vaccines targeting non-tumour antigens are potent immune modulators capable of sensitizing tumours to ICIs.

Improved survival with COVID-19 vaccination

To determine whether COVID-19 mRNA vaccines were associated with improved responses to immune checkpoint blockade, we first compared the OS among a cohort of patients with stage III/IV NSCLC treated at The University of Texas MD Anderson Cancer Center (MDACC) between January 2015 and September 2022 (Supplementary Table 1a). We identified 180 patients who received a COVID mRNA vaccine within 100 days of ICI initiation, and 704 patients who were treated with ICI and did not receive a COVID vaccine (Supplementary Table 1a). Of the 180 patients who received an mRNA vaccine within 100 days of ICI initiation, 117 received the BNT162b2 vaccine and 63 received mRNA-1273 (Extended Data Fig. 1a); 24 received a priming dose only, 57 received a booster only, 93 received both a prime and a boost dose, 5 received 2 booster doses, and 1 received a priming dose and 2 booster doses within 100 days of ICI initiation (Extended Data Fig. 1b); 81 received 1 dose of COVID-19 mRNA vaccination within 100 days, 98 received 2 doses, and 1 received 3 doses (Extended Data Fig. 1c). After controlling for 39 covariables with Cox proportional hazards regression, including clinical stage, histology, steroid use, performance status, mutation status, comorbidities and treatment year, we found that receipt of a COVID-19 mRNA vaccine within 100 days of initiation of ICI was associated with significantly improved median OS (20.6 months versus 37.3 months) and 3 year OS (30.8% versus 55.7%, adjusted hazard ratio (HR$_{adj}$ = 0.51, 95% confidence interval (CI) = 0.37–0.71, $P < 0.0001$) (Fig. 1a and Supplementary Tables 2 and 3). This survival advantage was similar for patients with stage III unresectable NSCLC (HR$_{adj}$ = 0.37, 95% CI = 0.16–0.89, $P = 0.0268$) (Fig. 1b and Supplementary Tables 4 and 5) and stage IV NSCLC (HR$_{adj}$ = 0.52, 95% CI = 0.37–0.74, $P = 0.0002$) (Fig. 1c and Supplementary Tables 6 and 7); patients who received mRNA vaccines from either vaccine manufacturer (Extended Data Fig. 1a); and patients who had or had not received a previous COVID-19 mRNA vaccine (Extended Data Fig. 1b). Patients who received two vaccines in the 100 days surrounding initiation of ICI experienced similar OS compared with those who received only one vaccine (Extended Data Fig. 1c). These results were also consistent when considering only those patients whose closest mRNA vaccine was within 100 days before their first ICI (Extended Data Fig. 1d), when narrowing the vaccination window to 50 instead of 100 days (Extended Data Fig. 1e), when restricting to only those patients treated during the pandemic (Extended Data Fig. 1f), after correcting for immortal time bias (Extended Data Fig. 1g) and with propensity score matching (PSM; Extended Data Fig. 1h,i). Patients who received a COVID-19 vaccine within 100 days of chemotherapy (a group that did not include targeted therapies owing to significant heterogeneity and limited patient numbers within different drug cohorts) but did not receive ICI had no detectable survival benefit (Extended Data Fig. 2a). Likewise, patients who received a pneumonia or influenza vaccine within 100 days of initiating ICI (Extended Data Fig. 2b–e) and those with resectable stage III tumours (Extended Data Fig. 2f,g) experienced no improvement in survival.

We then repeated this analysis in a separate cohort of patients treated with their first round of ICI for metastatic melanoma, including 43 patients who received a COVID-19 mRNA vaccine within 100 days of initiating ICI and 167 who did not receive a COVID-19 vaccine (Supplementary Table 1b). Of the patients who received mRNA vaccines,

21 received BNT162b2 and 22 received mRNA-1273 (Extended Data Fig. 3a); 6 received a priming dose only, 8 received a booster only, 16 received both a prime and a boost dose, and 13 received 2 booster doses during our period of interest, (Extended Data Fig. 3b); 14 received 1 dose of COVID-19 mRNA vaccination within 100 days, and 29 received 2 doses (Extended Data Fig. 3c). After accounting for covariables, including histology, steroid use, performance status, mutation status, comorbidities and treatment year with Cox proportional hazards regression, we found that receipt of a COVID-19 mRNA vaccine within 100 days of initiating ICI was associated with substantially improved OS (median OS, 26.67 months versus unmet; 36-month OS, 44.1% versus 67.6%; HR_{adj} = 0.37, 95% CI = 0.18–0.74, P = 0.0048) (Fig. 1d and Supplementary Tables 8 and 9) and progression-free survival (PFS) (median PFS, 4.0 months versus 10.3 months; 36-month PFS, 23.7% versus 39.5%; HR_{adj} = 0.63, 95% CI = 0.40–0.98, P = 0.0383) (Fig. 1e and Supplementary Tables 10 and 11). These effects were again similar for both vaccine manufacturers (Extended Data Fig. 3a), prime and boost vaccines (Extended Data Fig. 3b), patients receiving single or multiple vaccine doses (Extended Data Fig. 3c), when limiting the analysis to only patients who received their vaccine prior to initiating ICI (Extended Data Fig. 3d), when limiting the analysis to only those treated during the pandemic (Extended Data Fig. 3e,f) and when expanding the analysis to include patients on second- or third-line therapy and those without distant metastases (Extended Data Fig. 3g–i). Moreover, the survival advantage was magnified with PSM (OS: HR = 0.44, 95% CI = 0.18–0.77, P = 0.0063; PFS: HR = 0.46, 95% CI = 0.27–0.77, P = 0.0022) (Extended Data Fig. 3j,k).

Type I IFN mediates RNA vaccine immunity

To demonstrate whether effects observed in humans could be modelled in animals, we recreated commercial preparations of COVID mRNA vaccines for administration to tumour-bearing animals in conjunction with ICIs. As SARS-CoV-2 spike protein has been fully sequenced, we synthesized the published mRNA construct used for the Pfizer/BioNTech vaccine (BNT162b2) and validated the fidelity of synthesis based on mRNA size (Extended Data Fig. 4a,b) and the ability to elicit neutralizing antibodies after in vivo administration to animals (Extended Data Fig. 4c). mRNA was encapsulated in lipid nanoparticles (LNPs) and met the specification range delineated for clinical preparations of BNT162b2 based on encapsulation efficiency, size distribution, polydispersity and charge[18] (Extended Data Fig. 4d–g), the latter of which we found could be disproportionately affected by buffer conditions leading to a net positive charge (Extended Data Fig. 4h). We chose mouse B16F0 melanoma and Lewis lung carcinoma (LLC) as models to test immunogenicity and efficacy of spike RNA-LNP vaccines due to the effects of the vaccine in these clinical settings and because both tumour models are poorly responsive to ICIs. We first treated mice with two vaccine doses in conjunction with ICI treatment. We found this regimen to be superior to either monotherapy alone in mice with established B16F0 tumours with tumour volumes of about 80 mm^3 (Fig. 2a and Extended Data Fig. 5a), in mice with subcutaneous (s.c.) LLC (Fig. 2b and Extended Data Fig. 5b) and in mice with established s.c. LLC with tumour volumes around 100 mm^3 (Fig. 2c and Extended Data Fig. 5c). In mice with established LLC, we identified metastatic lesions in the lungs of untreated mice that were similar for monotherapy but significantly reduced with the combination treatment (Extended Data Fig. 5d,e). We also found that starting RNA-LNPs before ICI produced similar effects relative to concomitant treatment (Extended Data Fig. 5f). We next tested whether RNA-LNPs could reduce the growth of orthotopic intrapulmonary tumours. We implanted LLC cells orthotopically and administered treatment starting on day 3. In this model, the combination of RNA-LNPs and ICI resulted in superior inhibition of tumour growth as measured by lung weights (Extended Data Fig. 5g).

We next sought to understand the mechanism by which RNA-LNPs targeting the spike protein mediate these antitumour effects. To do this, we used an early treatment model of B16F0 with or without cytokine-blocking antibodies. In this model, RNA-LNPs and PD-L1 blockade each provided numerical but statistically insignificant survival benefits. However, combination therapy with RNA-LNPs and PD-L1 blockade strongly inhibited tumour growth (Fig. 2d and Extended Data Fig. 6a,b). Although we previously demonstrated a role for IFNα in the response to mRNA vaccines, recent evidence suggests a dominant role for IL-1 signalling in responses to the specific RNA-LNPs targeting the COVID-19 spike protein[15]. We therefore evaluated the importance of each pathway with antibodies blocking the IL-1 and IFNα receptors. While blockade of IL-1R had no effect on tumour growth, anti-tumour responses were completely abrogated when blocking type I interferon signalling with IFNAR1 monoclonal antibodies (Fig. 2d). Moreover, direct administration of supraphysiologic doses of type I IFN recapitulated the antitumour effects (Extended Data Fig. 6c). However, stimulation of type I IFN signalling with low molecular mass (LMW) poly(I:C) did not elicit similar immunity (Extended Data Fig. 6d). These results highlight the importance of IFN in driving innate and adaptive immunity, and the ability to manipulate and reset the immune setpoint away from tolerance toward effector immune responses in the presence of ICIs using a commercially available mRNA preparation.

Next, we sought to assess whether other mRNA species would elicit similar antitumour effects. We first modified the protein encoded by the mRNA by replacing the spike mRNA with mRNA encoding the cytomegalovirus antigen pp65, which is overexpressed in human glioma but not in B16F0. We found no significant difference in antitumour activity between these two groups, suggesting that innate immune sensing of the mRNA itself is the primary driver of antitumour activity from mRNA vaccines (Extended Data Fig. 6e,f).

As N^1-methyl-pseudouridine is used in place of uridine in COVID-19 mRNA vaccines to reduce innate immune activation, we hypothesized that replacing N^1-methyl-pseudouridine with uridine to activate pattern recognition receptors would provide even more robust innate immune activation and antitumour activity. As expected, replacing N^1-methyl-pseudouridine with uridine in *pp65* mRNA resulted in further synergy with ICI (Extended Data Fig. 6e,f). However, replacing N^1-methyl-pseudouridine with uridine in spike mRNA provided only numerical improvement in antitumour response (Extended Data Fig. 6e,f), suggesting that innate immune sensing is a multifactorial process that may be influenced by specific mRNA constructs.

We then completed additional studies to identify how RNA-LNPs elicit antitumour immunity. Previous work has established that RNA-LNPs stimulate type I IFN production by stimulating the intracellular double-stranded RNA (dsRNA) sensor MDA5[19]. However, the mechanism by which RNA-LNPs activate this sensor is unclear. To understand this further, we first ruled out a role for dsRNA in our vaccines by measuring the level of dsRNA contamination in our manufactured ssRNA product. We found the dsRNA/ssRNA ratio in our mRNA to be 0.011% (Extended Data Fig. 7a). We then repeated our tumour growth curve incorporating an additional dsRNA-removal protocol[20]. With this step, we successfully removed all detectable dsRNA contamination (Extended Data Fig. 7a). Importantly, we found no change in antitumour efficacy with the complete elimination of dsRNA using this method (Extended Data Fig. 7b). Finally, we found no abrogation of type I IFN after RNA-LNP administration in mice lacking RIG-I, a critical sensor of dsRNA and activator of type I IFN response (Extended Data Fig. 7c). Together, these data suggest that dsRNA is not a major cause of the antitumour effects in our preclinical models.

We next tested whether the specific LNP construct impacted antitumour immunity with the same mRNA input. We found that anionic lipoplexes formulated as lipid particle aggregates (LPA) do not elicit

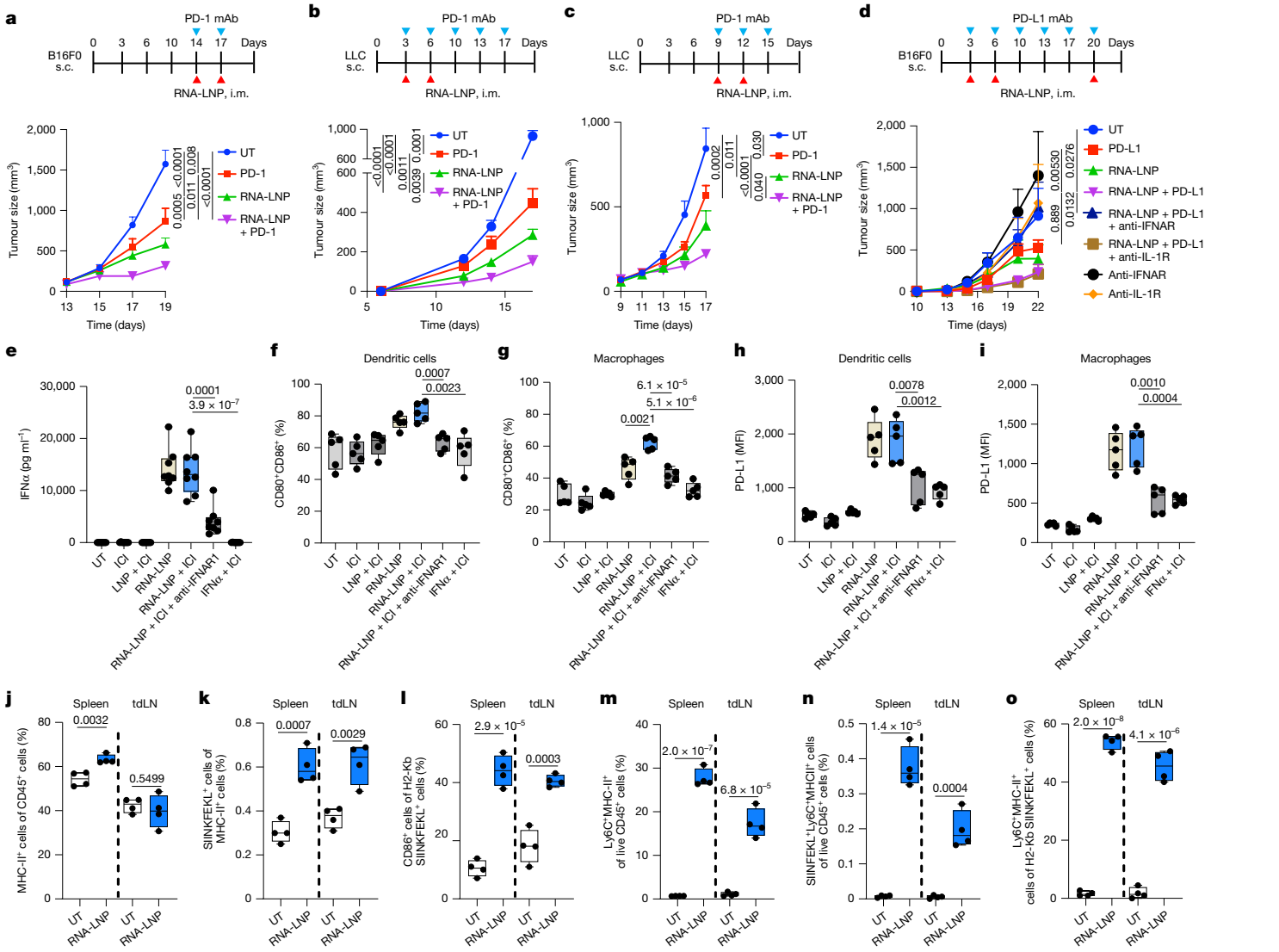

Fig. 2 | Spike RNA-LNPs prime anti-cancer immunity in an IFN-I dependent manner. a, The experimental design and tumour volume of mice inoculated with B16F0 cells. Groups included untreated (UT; $n = 7$), anti-PD-1 ($n = 8$), RNA-LNPs ($n = 8$) and RNA-LNPs + anti-PD-1 ($n = 8$). mAb, monoclonal antibody. **b**, The experimental design and tumour volume for mice inoculated with LLC cells. Groups included untreated ($n = 8$), anti-PD-1 ($n = 9$), RNA-LNP ($n = 9$) and RNA-LNPs + anti-PD-1 ($n = 9$). **c**, The experimental design and tumour volume measurements for mice inoculated with LLC cells. Groups included untreated ($n = 9$), anti-PD-1 ($n = 10$), RNA-LNP ($n = 7$) and RNA-LNPs + PD-1 ($n = 8$). **d**, The experimental design and tumour volume for mice inoculated with B16F0 cells. $n = 12$ per group. **e**, IFNα plasma enzyme linked immunosorbent assay (ELISA) from B16F0-tumour-bearing mice ($n = 8$ per group) 24 h after one RNA-LNP vaccine (day 3). **f**–**i**, Cellular phenotyping within 24 h of vaccine 3 (days 3, 6 and 20) of cells from spleens of mice bearing B16F0 tumours ($n = 5$ per group), including the percentage of activated ($CD80^+CD86^+$) DCs (**f**) and macrophages (**g**). **h**,**i**, PD-L1 median fluorescence intensity (MFI) on activated mature DCs (**h**) and macrophages (**i**). **j**–**o**, Characterization of antigen presentation among myeloid cells in tumour draining lymph nodes (tdLNs) and spleens of mice bearing B16F10-ova tumours 24 h after vaccine 2 (days 10 and 13). The overall percentage of $CD45^+$ cells that express MHC-II^+ (**j**), the percentage of MHC-II^+ cells presenting SIINFEKL (**k**), the percentage of SIINFEKL-presenting $MHCII^+$ cells that express the activation marker CD86 (**l**), the percentage of $CD45^+$ cells that are MHC-II^+Ly6C^+ (**m**), $SIINFEKL^+MHC\text{-}II^+Ly6C^+$ cells as a percentage of all $CD45^+$ cells (**n**) and $Ly6C^+MHCII^+$ cells as a percentage of total SIINFEKL-presenting cells (**o**) are shown. $n = 4$ biologically independent mice per group. Significance was determined using two-way analysis of variance (ANOVA)/mixed-effect analysis with Geisser–Greenhouse correction (**a**–**d**) and two-tailed unpaired *t*-tests (**e**–**o**). *n* indicates the number of biologically independent samples. For the box plots, the whiskers extend to the highest and lowest values, the box limits show the first and third quartiles and the centre line shows the median value. For **a**–**d**, data are mean ± s.e.m.

similar antitumour effects (Extended Data Fig. 7b). Given that previous literature described that higher-order RNA structures may also stimulate MDA5 activation[21], we hypothesized that RNA-LNPs might create higher order structures. Consistent with this hypothesis, we found that RNA extracted from our RNA-LNPs contained high-molecular-mass secondary structures similar in mass to dsRNA (Extended Data Fig. 7d and Supplementary Fig. 1). Combined with previous reports of MDA5 activation with RNA-LNPs but not with ssRNA alone, these data may suggest a mechanism by which encapsulation with LNPs forms high-molecular-mass secondary structures enabling activation of double-stranded sensing machinery (that is, MDA5) for induction of type I interferons.

RNA vaccines stimulate innate immunity

We next sought to better understand the impact of RNA-LNPs on innate immune cells. IFNα was significantly elevated in both RNA-LNP and combination groups in conjunction with other T helper 1 chemokines

(Fig. 2e and Extended Data Fig. 8). This surge in cytokine/chemokine response correlated with an increase in myeloid cell activation in the lymphoid organs of mice treated with RNA-LNP alone or in combination with ICI. After treatment with spike-encoding RNA-LNP, there was precipitous activation of APCs, including DCs, macrophages and Ly6C$^+$ cells expressing MHC class II (MHC-II) in lymphoreticular organs, that was abrogated by IFNAR1 blockade (Fig. 2f–i, Extended Data Fig. 9a,b, Supplementary Table 12 and Supplementary Fig. 2). Although this response was dependent on interferon signalling, the magnitude of the response could not be achieved by simply administering systemic IFNα in combination with ICI (Fig. 2f–i and Extended Data Fig. 9a,b).

Myeloid activation extended to the tumour, where receipt of RNA-LNPs was associated with IFNAR1-dependent increases in activated Ly6C$^+$ myeloid cells (Extended Data Fig. 9c and Supplementary Fig. 3). To determine whether increased myeloid activation corresponded to enhanced presentation of tumour antigens, we treated mice with B16F10 tumours expressing chicken ovalbumin (B16F10-OVA) at days 10 and 13 and evaluated presentation of ovalbumin on MHC-I using flow cytometry. We found that spike-encoding RNA-LNPs stimulate APCs to present tumour antigens in lymphoid organs in the presence of costimulatory molecules (Fig. 2j–l and Supplementary Fig. 4). Notably, presentation of tumour antigens in the presence of costimulatory molecules was particularly enriched in Ly6C$^+$MHC-II$^+$ cells (Fig. 2m–o).

RNA vaccines reprogram adaptive immunity

In addition to the precipitous activation of APCs, spike-encoding RNA-LNPs in combination with ICIs also elicited expansion of CD8$^+$ T lymphocytes with a marked increase in activation within the effector and effector memory compartments (Fig. 3a,b, Extended Data Fig. 9d, Supplementary Table 13 and Supplementary Fig. 5). Concomitant with these findings, PD-1 expression was increased in T cells and effector/effector memory CD8$^+$ cell subsets, underscoring the potent ability of combination therapy to rapidly prime T cells (Extended Data Fig. 9e,f and Supplementary Fig. 6). Overall, these results illustrate a role for systemic immunomodulation in the recruitment of myeloid cells to lymphoid organs for tumor antigen presentation to cognate T cells.

To confirm that spike RNA-LNPs were mediating the expansion of tumour reactive T cells, we isolated CD8$^+$ cells from spleens of treated mice and stained them with tetramers targeting peptides with high predicted binding affinity from six melanoma-associated antigens: GP-100 EGSRNQDWL, GP-100 KVPRNQDWL, claudin 6 (CLDN6), survivin, WT1 and Trp2. We found that combination therapy with RNA-LNPs and ICIs stimulated expansion of tetramer reactive T cells targeting each of these antigens (Fig. 3c and Supplementary Fig. 7). To confirm that these T cells were truly tumour reactive, we used an activation-inducible marker (AIM) assay[22,23]. In this assay, antigen-reactive T cells cultured ex vivo with overlapping peptide pools from the same tumour antigens are identified through tandem expression of the AIMs CD69 and 4-1BB (Supplementary Fig. 8 and Supplementary Table 14). Using this approach, we detected a substantial increase in peptide-reactive (AIM$^+$) CD8$^+$ T cells from mice treated with the combination of RNA-LNPs and ICI, further supporting tumour reactivity (Fig. 3d). These data confirm that spike RNA-LNPs prime the immune response for activation, presentation and recognition of tumour-associated antigens in a manner that can be significantly expanded through concomitant treatment with ICI.

RNA vaccines induce T cell infiltration

We next evaluated the T cell compartment in treated tumours. In mice with B16F0 tumours, we identified substantial infiltration of PD-1$^+$CD8$^+$ T cells using both immunofluorescence (Fig. 3e,f, Supplementary Fig. 6 and Supplementary Table 15) and flow cytometry (Fig. 3g). Importantly, we found that treatment with RNA-LNPs and ICIs increased PD-1 expression on total tumour-infiltrating CD8$^+$ cells by greater than twentyfold (2.39% versus 51.363%, $P < 0.0001$) (Fig. 3f), and that PD-1$^+$CD8$^+$ T cells dominated the total CD3$^+$ T cell compartment in treated mice while representing only a small minority of total CD3$^+$ T cells in untreated mice (5.69% versus 60.6%, $P < 0.001$) (Fig. 3g). We next evaluated the antigen specificity of these cells. As there were many fewer CD8$^+$ T cells in tumours compared with in spleens after enriching CD8$^+$ cells, we pooled the six tetramers described above for a single pan-tetramer stain containing all six targets. Using this approach, we found that CD8$^+$ tumour-infiltrating lymphocytes from mice treated with RNA-LNPs and ICIs were twice as likely to be tetramer reactive compared with non-RNA-LNP controls (3.10% versus 7.98%, $P = 0.0229$) (Fig. 3h and Supplementary Fig. 7).

Commensurate with the increase in tumour-reactive T lymphocytes in the TME, we found that spike-encoding RNA-LNPs significantly increased PD-L1 expression on tumour cells (Fig. 3i–k, Extended Data Fig. 9g,h and Supplementary Figs. 9 and 10). Blockade of IFNα signalling abrogated PD-L1 expression, confirming its importance in initiating the immunotherapy response (Extended Data Fig. 9g,h). Together, these data suggest that spike RNA-LNPs stimulate the production and infiltration of activated, tumour-reactive CD8$^+$ T cells that overcome compensatory expression of PD-1 and PD-L1 in the presence of ICIs.

COVID-19 vaccines shape immunity in humans

As there are species-specific differences in how humans and mice respond to mRNA, we next sought to confirm that the pathways identified in mouse models are relevant in humans. To do this, we collected blood and plasma samples from five healthy volunteers at the baseline and at 6 h, 24 h, 7 days and 14 days after receipt of mRNA-1273 Spikevax Monovalent XBB.1.5 (COVID-19 mRNA vaccine, 2023–2024 formulation, 50 μg mRNA) (Fig. 4a). We first evaluated plasma from these volunteers using the NULISA-Seq Inflammation Panel (Alamar Biosciences)—a multiplex assay designed to sensitively detect over 250 immune-related cytokines. As IFNα was found to be essential for antitumour activity in mice, we were particularly interested in the kinetics of this protein at 24 h. Notably, not only was IFNα upregulated, but it was the most upregulated cytokine at any timepoint, increasing by an average of around 280-fold relative to the baseline to a final plasma concentration between 1 and 10 pg ml^{-1} (Fig. 4b,c). More broadly, IL-6 and IFNγ were the only cytokines that were significantly elevated at 6 h after immunization (Fig. 4d). By contrast, a multitude of inflammatory cytokines surged at 24 h after immunization, including IFNα, IFNγ, IFNω and IFNγ-inducible protein-10 (CXCL10) (Fig. 4d and Supplementary Fig. 11). Although IL-1 was not found to be significantly increased at any timepoint, IL-1R antagonist (IL1RN) was significantly elevated at 24 h, suggesting a compensatory response to a surge in IL-1 (Fig. 4d). As expected, cytokine responses to COVID-19 mRNA vaccination were short-lived in healthy individuals, with all cytokines returning to the baseline levels by 7 days (Fig. 4d).

To evaluate the impact of COVID-19 mRNA-induced antiviral cytokines on immune cells, we next evaluated the phenotypes of circulating myeloid cells using flow cytometry. Consistent with our findings in mouse models, we found that mRNA immunization drove innate immune activation exemplified by increased expression of PD-L1 on circulating CD11b$^+$ myeloid cells and CD11c$^+$ DCs (Fig. 4e,f, Supplementary Table 16 and Supplementary Fig. 12). Vaccination was also associated with activation of natural killer cells exemplified by a doubling of expression of IL-2Rα (also known as CD25) on CD56^{high} cells (Fig. 4g) and circulating T cells exhibited by a doubling of expression of CD69 (Fig. 4h, Supplementary Table 17 and Supplementary Fig. 13). Phenotypes for all cells normalized by 7 days, which may be a result of the lack of target in these healthy participants or

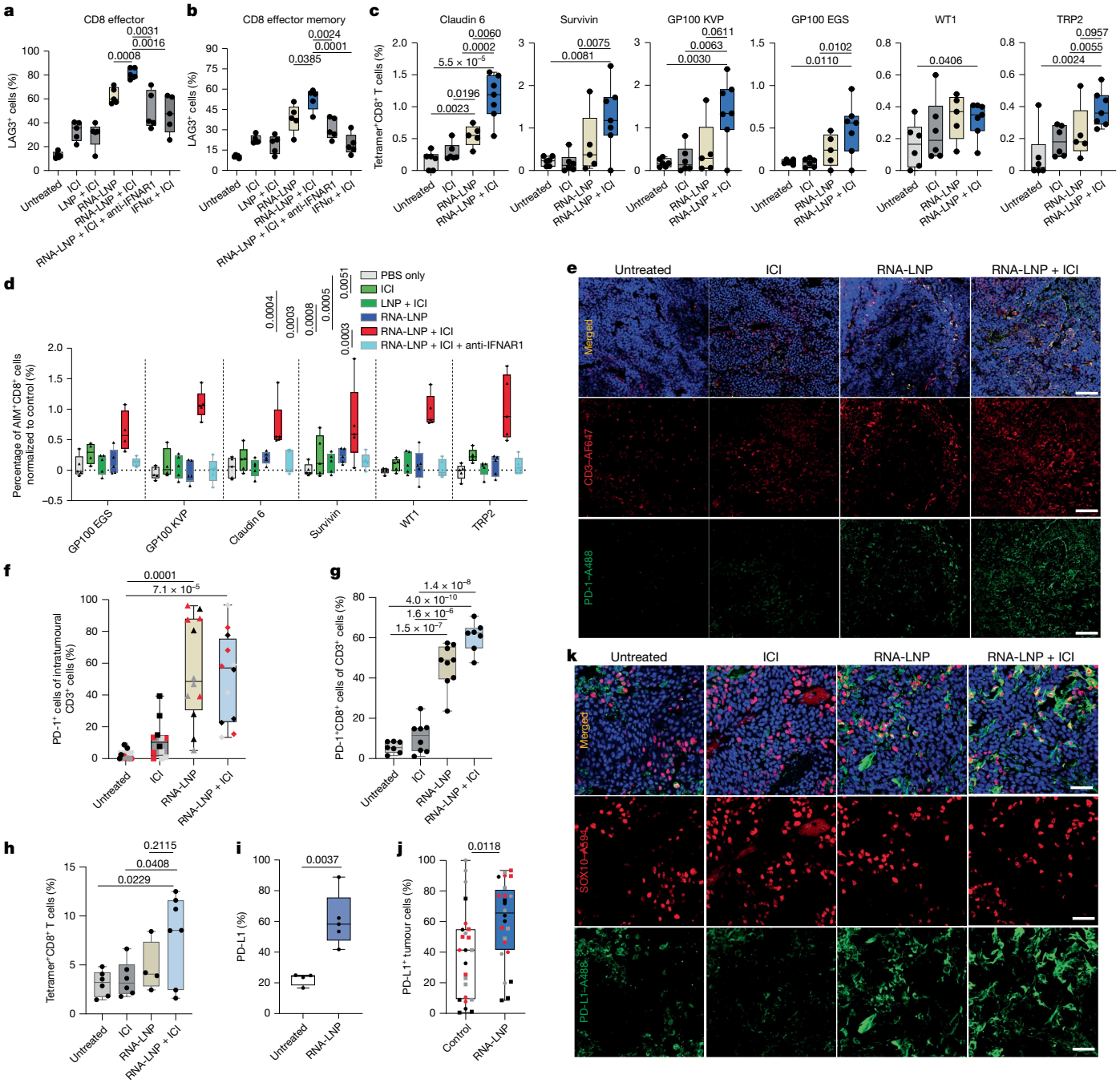

Fig. 3 | Spike RNA-LNPs generate tumour-reactive T cells and increase PD-L1 expression on tumour cells. a,**b**, The percentage of activated effector (**a**) and effector memory (**b**) T cells in the spleens of tumour-bearing mice on day 21 (vaccine days 3, 6, 17) ($n = 5$ per group). **c**, The percentage of tetramer$^+$ cells of splenic CD8$^+$ T cells collected from mice bearing B16F0 tumours on day 21 (vaccination days 14 and 17). Groups include untreated ($n = 6$), anti-PD-1 ($n = 6$), RNA-LNPs ($n = 5$) and RNA-LNPs + anti-PD-1 ($n = 7$). **d**, The normalized percentage of AIM$^+$ T cells ($n = 5$ mice per peptide; exceptions are shown in the Supplementary Information) after splenocyte co-culture with overlapping peptide pools. **e**,**f**, Representative images (**e**) and blinded manual counting ($n = 4$ tumours per group with 4 counts per tumour) (**f**) of PD-1$^+$CD3$^+$ cells by immunofluorescence 24 h after vaccine 3 (days 3, 6 and 20) from s.c. tumors of B16F0-tumour-bearing mice treated with or without anti-PD-L1. For **e**, scale bars, 100 µm. AF647, Alexa Fluor 647. **g**, The percentage PD-1$^+$CD8$^+$ cells of CD3$^+$ T cells in tumours of B16F0-bearing mice vaccinated with RNA-LNPs (days 14 and 17). Groups included untreated ($n = 7$), anti-PD-L1 ($n = 8$), RNA-LNPs ($n = 9$) and RNA-LNPs + anti-PD-L1 ($n = 7$). **h**, Pooled tetramer positivity (%) among CD8$^+$ T cells in B16F0 tumours. Groups included untreated ($n = 6$), anti-PD-1 ($n = 6$), RNA-LNPs ($n = 4$) and RNA-LNPs + anti-PD-1 ($n = 7$) (RNA-LNPs days 14 and 17). **i**, PD-L1 expression on B16F0 tumour cells (CD45$^-$FSC-A^{high}) isolated from mice 24 h after vaccine 3 (days 3, 6 and 17) as determined using flow cytometry. Groups included untreated ($n = 4$) and RNA-LNPs ($n = 5$). **j**,**k**, Blinded manual counting ($n = 6$ tumours per group with 4 counts per tumour) (**j**) and representative images (**k**) of PD-L1$^+$ tumour cells (SOX10) by immunofluorescence 24 h after vaccine 3 (days 3, 6, 21) from B16F0-tumour-bearing mice. For **k**, scale bars, 50 µm. For **j**, the circle symbols indicate PBS treatment and the square symbols represent anti-PD-L1 treatment. For **f** and **j**, the colours represent individual tumours. Significance was determined using two-tailed unpaired *t*-tests (**a**–**c** and **g**–**j**), two-tailed Welch's *t*-test (**f**), and two-tailed Brown–Forsythe and Welch ANOVA, followed by Dunnett's T3 multiple-comparison test (**d**). For the box plots, the whiskers extend to the highest and lowest values, the box limits show the first and third quartiles and the centre line shows the median value. *n* values indicate biologically independent samples unless indicated otherwise.

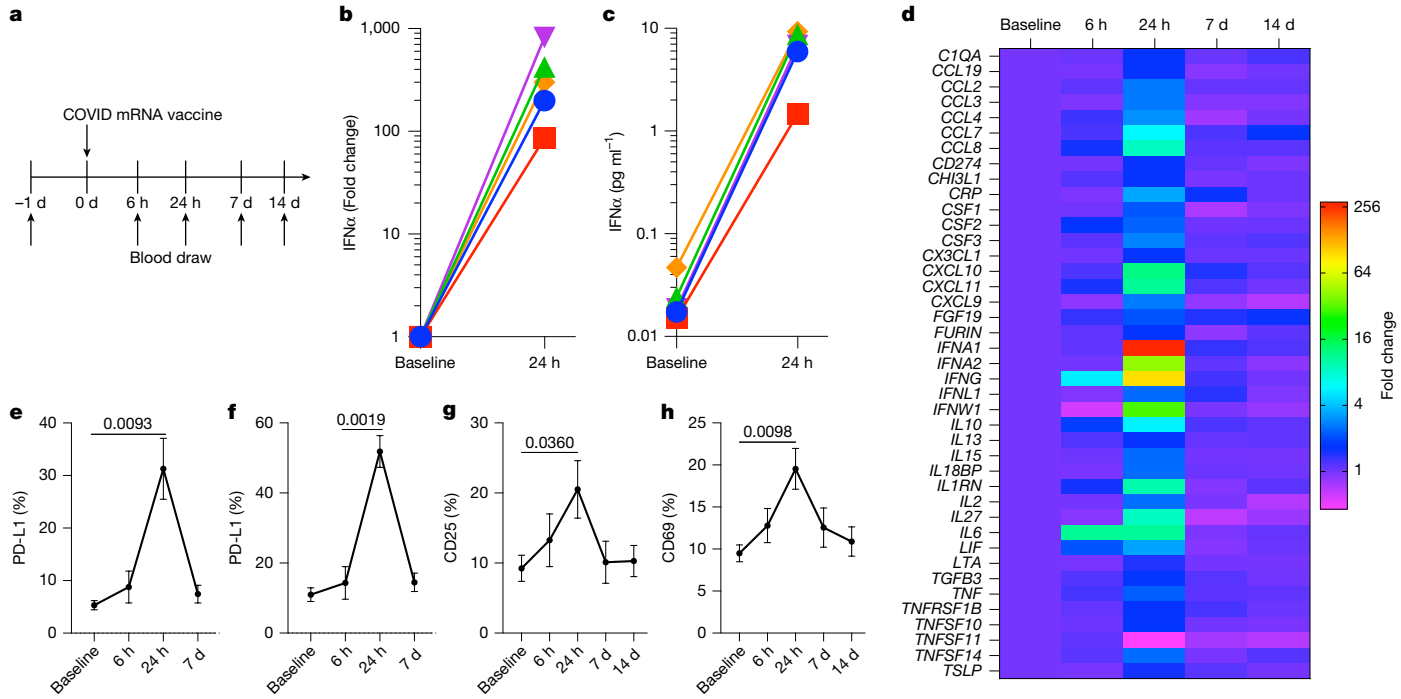

Fig. 4 | COVID-19 mRNA vaccines generate a surge in IFNα, innate immune activation and adaptive immunity in humans. a, Schematic of the experimental design in which blood was drawn from five healthy individuals at baseline and 6 h, 24 h, 7 days and 14 days after Spikevax (mRNA-1273) COVID-19 mRNA immunization. **b**,**c**, Individual datapoints highlighting changes in expression of IFNα from baseline to 24 h for each of five healthy volunteers. Data are expressed as the fold change measured using the NULISAseq Inflammation Panel (**b**). The concentration was also measured separately with NULISAseq absolute quantification (AQ) (**c**). **d**, Dynamic expression of the cytokines that are significantly elevated at 24 h at 6 h, 24 h, 7 days and 14 days after COVID-19 mRNA vaccination. Significant variables were defined as those with $P < 0.05$ and a $\log_2$-transformed fold change with an absolute value of greater than 0.5 after linear modelling with fixed effects. Adjusted P values were calculated using moderated two-tailed t-tests with false-discovery rate (FDR) correction for multiple testing. **e**,**f**, PD-L1 expression on circulating myeloid cells ($CD3^-CD19^-CD56^-CD11b^+$) ($n = 5$) (**e**) and DCs ($CD3^-CD19^-CD56^-CD11c^+MHC\text{-}II^+$) ($n = 5$) (**f**) at 6 h, 24 h and 7 days after immunization. **g**,**h**, Activation of natural killer cells ($CD56^+$; $n = 5$) (**g**), and T cells expressed as numbers of $CD69^+$ cells of $CD8^+CD3^+$ cells ($n = 5$) (**h**) at 6 h, 24 h, 7 days and 14 days after immunization. Data are mean ± s.e.m. P values were calculated using two-tailed paired t-tests.

lymphoreticular localization of activated T cells for polarization into memory cells.

We next repeated this study in 11 healthy volunteers who received the Comirnaty vaccine (BNT162b2, COVID-19 mRNA vaccine, 2024–2025 formula, with 30 µg mRNA) (Extended Data Fig. 10a–h). Although we found similar changes to the cytokine profile overall, the magnitude of the increase in type I IFN and innate immune activation by flow cytometry was significantly reduced with BNT162b2, which contains less mRNA relative to mRNA-1273 (Extended Data Fig. 10b–i).

RNA vaccines amplify PD-L1 in NSCLC

As infiltration of antigen-specific T cells in tumours is known to be associated with increases in PD-L1 expression on tumour cells and was correlated with antitumour response in our preclinical models, we hypothesized that patients who received a COVID-19 mRNA vaccine would exhibit higher PD-L1 expression on their tumours. To test this hypothesis, we assembled two cohorts. We first evaluated 2,315 pathology reports from patients with NSCLC with biopsies reporting tumour proportion score (TPS), separating patients into three groups based on the timing between their biopsy and their most recent mRNA vaccine (Fig. 5a). We found that patients who had received a COVID-19 mRNA vaccine less than 100 days before biopsy exhibited a 24% increase in mean TPS of PD-L1 compared with patients who had not received any COVID-19 mRNA vaccines before biopsy (31% versus 25%, $P = 0.0450$) and a 41% increase in mean TPS relative to patients who received an mRNA vaccine 100 or more days before biopsy (31% versus 22%, $P = 0.0099$) (Fig. 5b and Extended Data Fig. 10j). As a TPS of 50% is a clinically important threshold to determine whether patients with NSCLC are eligible for single-agent immunotherapy instead of chemo-immunotherapy, we next evaluated these data as a binary outcome around this threshold. Notably, we found that patients who received a COVID-19 mRNA vaccine were 29% more likely to meet or exceed the 50% TPS threshold over unvaccinated patients (36% versus 28%, $P = 0.0295$) (Fig. 5c), suggesting that mRNA vaccines have a sufficient impact on TPS to modify treatment decisions. By contrast, pre-biopsy influenza and pneumonia vaccines were not associated with TPS changes (Fig. 5d).

RNA vaccines amplify tumour PD-L1 broadly

To expand our findings beyond NSCLC and melanoma, we assembled a separate cohort including all patients at our quaternary referral centre with pathology reports including the term ‘PD-L1’ in a four-year period including the pandemic era (Fig. 5e). Together, we identified 5,317 unique pathology reports from January 2020 to October 2023 with the term ‘PD-L1’ including 2,831 reporting TPS from a diverse array of patients representing a variety of primary sites and histologies (Fig. 5f). In this cohort, receipt of a COVID-19 mRNA vaccine within 100 days before biopsy was associated with a 37% increase in TPS (13.3% versus 9.7%, $P = 0.0364$) (Fig. 5g and Extended Data Fig. 10k), similar to the effect seen in patients with NSCLC. As in the NSCLC cohort, influenza vaccines were not associated with similar increases in TPS (Fig. 5h). We next repeated the survival analysis in this broad patient cohort, including patients at our institution with a biopsy for PD-L1 during our dates of interest who received ICI ($n = 888$). In this cohort, patients who received any COVID-19 vaccine within 100 days of initiating ICI experienced significantly improved survival relative to

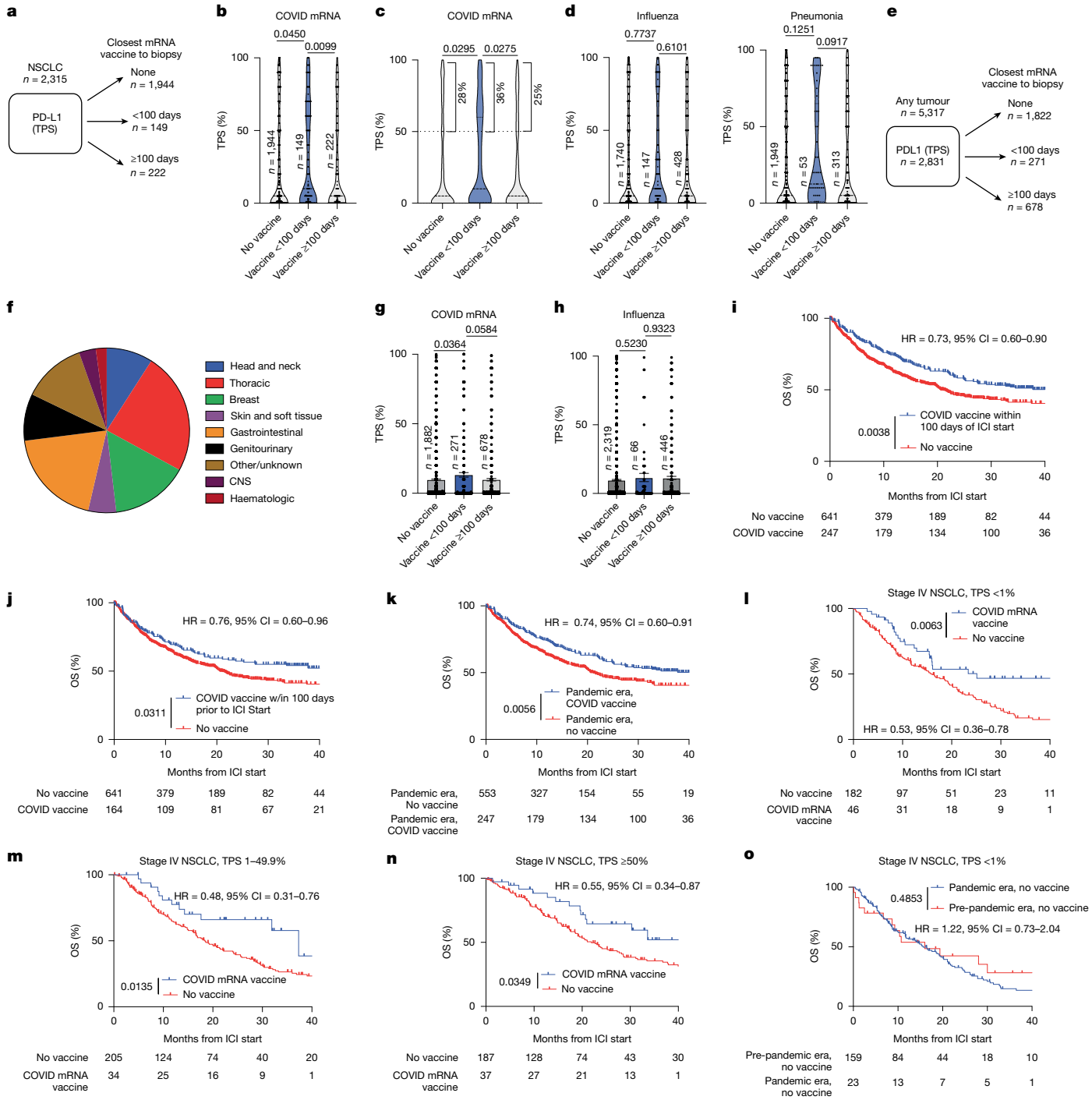

Fig. 5 | COVID-19 mRNA vaccines are associated with increased PD-L1 expression on tumours and improved clinical outcomes across a broad set of tumour histologies. a, Schematic of patients with NSCLC biopsies documenting PD-L1 TPS. **b**, TPS stratified by COVID-19 mRNA vaccination timing. **c**, The distribution of samples with TPS ≥ 50%. **d**, TPS stratified by influenza (left) or pneumonia (right) vaccination timing. **e**, Schematic of biopsies documenting TPS or combined positive score (CPS) of PD-L1 at our institution (January 2020 to October 2023). **f**, Primary tumour locations from this diverse cohort. **g**, TPS in the tissue-agnostic cohort stratified by COVID-19 mRNA immunization timing. **h**, TPS stratified by timing of influenza vaccination. *P* values were calculated using two-tailed unpaired *t*-tests (**b**, **d** and **h**), two-tailed unpaired *t*-tests with Welch's correction for unequal variance (**g**) and two-sided Fisher's exact test evaluating the likelihood of TPS greater than 50% (**c**). The violin plots show the distribution of data with individual datapoints included. **i**, Survival of patients in the tissue-agnostic cohort treated with ICI who received any COVID-19 vaccine within 100 days of initiating ICI or did not receive any COVID-19 vaccine. **j**, Survival of patients in **i** stratified by receipt of COVID-19 vaccine before ICI. **k**, Survival for patients in **i** who started ICI in the pandemic era (since 2 September 2020, 100 days before mRNA vaccine approval). Survival analyses in the tissue-agnostic cohort were not limited to only those patients with a clear TPS value. **l**–**o**, The OS for patients with metastatic stage IV NSCLC treated with ICI who received a COVID-19 mRNA vaccine within 100 days of initiating ICI or did not receive a COVID-19 vaccine who had baseline PD-L1 expression at baseline biopsy TPS < 1% (**l**), 1–49.9% (**m**) or ≥50% (**n**). To evaluate the impact of vaccination in each clinical setting, patients were excluded if they received a COVID-19 mRNA vaccine before their biopsy. **o**, OS of unvaccinated patients with stage IV NSCLC stratified by era of ICI start who had baseline TPS < 1% at biopsy. *P* values and HRs were calculated using log-rank (Mantel–Cox, two-sided) tests (**i**–**o**).

their unvaccinated peers ($P = 0.0038$, HR = 0.73, 95% CI = 0.60–0.90) (Fig. 5i). This effect was consistent when limited to patients who received their vaccine within 100 days before the start of ICI ($P = 0.0311$, HR = 0.76, 95% CI = 0.60–0.96) (Fig. 5j) and patients who started their ICI during the pandemic era ($P = 0.0056$, HR = 0.74, 95% CI = 0.60–0.91) (Fig. 5k).

RNA vaccines boost ICIs in cold tumours

We next sought to evaluate whether vaccination could restore immune sensitivity in patients with immunologically 'cold' tumors. We used pre-vaccine TPS as a surrogate for immune sensitivity, as NSCLC patients with TPS <1% have reduced benefit from ICIs compared to patients with baseline TPS >1%. Among patients with stage IV NSCLC and baseline TPS <1%, those who received a COVID-19 mRNA vaccine within 100 days of initiating ICI exhibited OS similar to that of patients with baseline TPS >1%, suggesting restored sensitivity to ICIs (Fig. 5l). In addition, the association between COVID-19 mRNA vaccination and OS was similar for patients with TPS <1% relative to those patients with a TPS at biopsy of 1–49.9% or ≥50% (Fig. 5l–n). This effect was not explained by changes in patient management during the pandemic period, as patients with stage IV NSCLC with TPS < 1% at biopsy who did not receive a vaccine had similar outcomes before and during the pandemic era (Fig. 5o).

Together, these data suggest a model in which mRNA vaccines targeting non-tumour-related antigens stimulate robust antitumour immune responses that sensitize tumors to ICIs (Extended Data Fig. 11). mRNA vaccines first stimulate a surge in antiviral cytokines, including IFNα, that drive systemic innate immune activation. Tumour-resident innate immune cells activated by this cytokine surge prime T cells, which become activated and infiltrate tumours. Although tumour cells evade attack by upregulating PD-L1 expression, combination with ICI enables COVID-19 mRNA vaccines to overcome this compensatory response, eliciting tumour regression and improved survival.

Discussion

Immunotherapy promises to deliver systemic anti-cancer therapy with long-term memory preventing recurrence. However, immunotherapy with ICIs relies on pre-existing anti-cancer immunity, which is absent in most patients. mRNA vaccines have recently emerged as a promising strategy to generate anti-cancer immunity to magnify the effects of ICIs[24–27]. Here we used mRNA vaccines targeting the COVID-19 spike protein to demonstrate a mechanism by which mRNA vaccines improve survival in combination with ICI, even when the mRNA does not encode tumour antigens. Spike RNA-LNPs elicit body-wide APC activation, leading to the expansion of highly activated tumour specific T cells. When combined with ICIs, these T cells mediate tumour regression. As personalized neoantigen vaccines require considerable manufacturing time, off-the-shelf RNA-LNPs targeting tumour-associated or even infectious disease antigens may represent widely available, low-cost alternatives for patients waiting for personalized neoantigen vaccines or in settings in which personalized neoantigen vaccines are not available.

Although the local injection of RNA-LNPs for infectious disease or personalized cancer vaccines does not aim to directly modify the tumour immune microenvironment, we show here that even local injection of RNA-LNPs containing N^1-methyl-pseudouridine to minimize innate immune activation produces sufficient stimulus to reprogram TMEs and sensitize tumours to ICI. Moreover, we find that augmenting innate immune activation by replacing N^1-methyl-pseudouridine-modified mRNA with unmodified mRNA may further enhance the antitumour effects of this approach. The surprising effectiveness of this approach may explain the relative success of mRNA vaccines compared with other methodologies that also generate T cells reactive against targeted neoepitopes[10–13,28,29].

We show that COVID-19 mRNA vaccines increase PD-L1 expression on tumours, rendering immunologically cold tumours sensitive to ICIs. These results reveal that the timing of a routine immunization might influence treatment trajectories, and provide an over-the-counter means to overcome intrinsic ICI resistance. More broadly, they establish systemic innate immune modulation as a strategy to sensitize tumours to ICIs, and position off-the-shelf RNA therapeutics targeting infectious disease antigens as universal modulators of antitumour immunity.

These findings define a role for widely available vaccines for enhancing the efficacy of cancer immunotherapy. Although we focus on a single therapeutic due to its wide availability, these data could pave the way for other universal mRNA therapeutics specifically designed to reset patient immune systems for enhanced response to immunotherapy.

Online content

Any methods, additional references, Nature Portfolio reporting summaries, source data, extended data, supplementary information, acknowledgements, peer review information; details of author contributions and competing interests; and statements of data and code availability are available at https://doi.org/10.1038/s41586-025-09655-y.

1. Pires da Silva, I. et al. Ipilimumab alone or ipilimumab plus anti-PD-1 therapy in patients with metastatic melanoma resistant to anti-PD-(L)1 monotherapy: a multicentre, retrospective, cohort study. *Lancet Oncol.* **22**, 836–847 (2021).
2. Geoerger, B. et al. Pembrolizumab in paediatric patients with advanced melanoma or a PD-L1-positive, advanced, relapsed, or refractory solid tumour or lymphoma (KEYNOTE-051): interim analysis of an open-label, single-arm, phase 1-2 trial. *Lancet Oncol.* **21**, 121–133 (2020).
3. Schachter, J. et al. Pembrolizumab versus ipilimumab for advanced melanoma: final overall survival results of a multicentre, randomised, open-label phase 3 study (KEYNOTE-006). *Lancet* **390**, 1853–1862 (2017).
4. Borghaei, H. et al. Nivolumab versus docetaxel in advanced nonsquamous non-small-cell lung cancer. *N. Engl. J. Med.* **373**, 1627–1639 (2015).
5. Carbone, D. P. et al. First-line nivolumab in stage IV or recurrent non-small-cell lung cancer. *N. Engl. J. Med.* **376**, 2415–2426 (2017).
6. Fehrenbacher, L. et al. Atezolizumab versus docetaxel for patients with previously treated non-small-cell lung cancer (POPLAR): a multicentre, open-label, phase 2 randomised controlled trial. *Lancet* **387**, 1837–1846 (2016).
7. Garon, E. B. et al. Pembrolizumab for the treatment of non-small-cell lung cancer. *N. Engl. J. Med.* **372**, 2018–2028 (2015).
8. Herbst, R. S. et al. Pembrolizumab versus docetaxel for previously treated, PD-L1-positive, advanced non-small-cell lung cancer (KEYNOTE-010): a randomised controlled trial. *Lancet* **387**, 1540–1550 (2016).
9. Rittmeyer, A. et al. Atezolizumab versus docetaxel in patients with previously treated non-small-cell lung cancer (OAK): a phase 3, open-label, multicentre randomised controlled trial. *Lancet* **389**, 255–265 (2017).
10. Sayour, E. J. et al. Personalized tumor rna loaded lipid-nanoparticles prime the systemic and intratumoral milieu for response to cancer immunotherapy. *Nano Lett.* **18**, 6195–6206 (2018).
11. Sayour E. J. et al. Systemic activation of antigen presenting cells via RNA-loaded nanoparticles. *OncoImmunology* https://doi.org/10.1080/2162402X.2016.1256527 (2016).
12. Mendez-Gomez, H. R. et al. RNA aggregates harness the danger response for potent cancer immunotherapy. *Cell.* **187**, 2521–2535 (2024).
13. Kranz, L. M. et al. Systemic RNA delivery to dendritic cells exploits antiviral defence for cancer immunotherapy. *Nature* **534**, 396–401 (2016).
14. Qdaisat S. et al. Sensitization of tumours to immunotherapy by boosting early type-I interferon responses enables epitope spreading. *Nat. Biomed. Eng.* https://doi.org/10.1038/s41551-025-01380-1 (2025).
15. Tahtinen, S. et al. IL-1 and IL-1ra are key regulators of the inflammatory response to RNA vaccines. *Nat. Immunol.* **23**, 532–542 (2022).
16. Sousa L. G. et al. Spontaneous tumor regression following COVID-19 vaccination. *J. Immunother. Cancer* https://doi.org/10.1136/jitc-2021-004371 (2022).
17. Bafaloukos D. et al. Therapeutic effect of mRNA SARS-CoV-2 vaccine on melanoma skin metastases. *Vaccines* **10**, 525 (2022).
18. Szebeni, J. et al. Insights into the structure of comirnaty COVID-19 vaccine: a theory on soft, partially bilayer-covered nanoparticles with hydrogen bond-stabilized mRNA-lipid complexes. *ACS Nano* **17**, 13147–13157 (2023).
19. Li, C. et al. Mechanisms of innate and adaptive immunity to the Pfizer-BioNTech BNT162b2 vaccine. *Nat. Immunol.* **23**, 543–555 (2022).
20. Baiersdorfer, M. et al. A facile method for the removal of dsRNA contaminant from in vitro-transcribed mRNA. *Mol. Ther. Nucleic Acids.* **15**, 26–35 (2019).
21. Pichlmair, A. et al. Activation of MDA5 requires higher-order RNA structures generated during virus infection. *J. Virol.* **83**, 10761–10769 (2009).
22. Balmas E. et al. Islet-autoreactive $CD4^+$ T cells are linked with response to alefacept in type 1 diabetes. *JCI Insight* https://doi.org/10.1172/jci.insight.167881 (2023).
23. Poloni, C. et al. T-cell activation-induced marker assays in health and disease. *Immunol. Cell Biol.* **101**, 491–503 (2023).

24. Acar, R. et al. Treatment options in primary mediastinal B cell lymphoma patients, retrospective multicentric analysis; a Turkish oncology group study. *J. Cancer Res. Ther.* **19**, S138–S144 (2023).
25. Munoz, F. M. et al. Evaluation of BNT162b2 COVID-19 vaccine in children younger than 5 years of age. *N. Engl. J. Med.* **388**, 621–634 (2023).
26. Simoes, E. A. F. et al. Immunogenicity and safety of a third COVID-19 BNT162b2 mRNA vaccine dose in 5- to 11-year olds. *J. Pediatr. Infect. Dis. Soc.* **12**, 234–238 (2023).
27. Verbeke, R., Lentacker, I., De Smedt, S. C. & Dewitte, H. The dawn of mRNA vaccines: the COVID-19 case. *J. Control. Release* **333**, 511–520 (2021).
28. Baharom, F. et al. Systemic vaccination induces CD8$^+$ T cells and remodels the tumor microenvironment. *Cell.* **185**, 4317–4332 (2022).
29. Ramirez-Valdez, R. A. et al. Intravenous heterologous prime-boost vaccination activates innate and adaptive immunity to promote tumor regression. *Cell Rep.* **42**, 112599 (2023).

[1]Department of Radiation Oncology, Division of Radiation Oncology, The University of Texas MD Anderson Cancer Center, Houston, TX, USA. [2]Lillian S. Wells Department of Neurosurgery, Preston A. Wells, Jr. Center for Brain Tumor Therapy, McKnight Brain Institute, University of Florida, Gainesville, FL, USA. [3]McGovern Medical School, Houston, TX, USA. [4]Department of Enterprise Data Engineering and Analytics, The University of Texas MD Anderson Cancer Center, Houston, TX, USA. [5]Department of Neurosurgery, The University of Texas MD Anderson Cancer Center, Houston, TX, USA. [6]Brain Tumor Center, The University of Texas MD Anderson Cancer Center, Houston, TX, USA. [7]Department of Pediatrics, Division of Hematology-Oncology, University of Florida, Gainesville, FL, USA. [8]Department of Dermatology, Baylor College of Medicine, Houston, TX, USA. [9]Department of Pathology, Stanford University, Stanford, CA, USA. [10]Department of Thoracic Imaging, The University of Texas MD Anderson Cancer Center, Houston, TX, USA. [11]Scripps Health, San Diego, CA, USA. [12]University of North Carolina, Chapel Hill, NC, USA. [13]Department of Surgical Oncology, Division Surgery, The University of Texas MD Anderson Cancer Center, Houston, TX, USA. [14]Department of Thoracic/Head & Neck Medical Oncology, The University of Texas MD Anderson Cancer Center, Houston, TX, USA. [15]Department of Thoracic and Cardiovascular Surgery, The University of Texas MD Anderson Cancer Center, Houston, TX, USA. [16]Department of Genitourinary Medical Oncology, The University of Texas MD Anderson Cancer Center, Houston, TX, USA. [17]Data-Driven Determinants for COVID-19 Oncology Discovery Effort (D3CODE) Team, The University of Texas MD Anderson Cancer Center, Houston, TX, USA. [18]Department of Biostatistics, The University of Texas MD Anderson Cancer Center, Houston, TX, USA. [19]Department of Biostatistics, The University of Florida, Gainesville, FL, USA. [20]Department of Immunology, The University of Texas MD Anderson Cancer Center, Houston, TX, USA. [21]James P. Allison Institute, The University of Texas MD Anderson Cancer Center, Houston, TX, USA. [29]These authors contributed equally: Adam J. Grippin, Christiano Marconi, Sage Copling, Nan Li. [30]These authors jointly supervised this work: Elias J. Sayour, Steven H. Lin.

D3CODE Team

Ashley Aaroe[22], Sanu Abraham[22], Lee Andrews II[22], Kiran K. Badami[22], Janna A. Baganz[22], Pratibha Bajwa[22], Gregory R. Barbosa[22], Hannah C. Beird[22], Kristy Brock[22], Elizabeth M. Burton[22], Juan Cata[22], Caroline Chung[22], Catherine Claussen[22], John Crommett[22], Michael Cutherell[22], Bouthaina Dabaja[22], Hiba Dagher[22], Kevin M. Daniels[22], Mary Domask[22], Giulio Draetta[22], Paul Edelkamp Jr[22], Sarah Fisher[22], Katy Elizabeth French[22], Andrew Futreal[22], Maria Gaeta[22], Myrna Godoy[22], Drew Goldstein[22], Jillian Gunther[22], Kate Hutcheson[22], David Jaffray[22], Jeff Jin[22], Teny Matthew John[22], Trey Kell[22], Mark Knafl[22], Rayson C. Kwan[22], J. Jack Lee[22], Jennifer Litton[22], Kevin W. McEnery[22], Mary McGuire[22], Benjamin Mescher[22], Tejo Musunuru[22], Mayoora Muthu[22], Joseph Nates[22], Craig S. Owen[22], Priyadharshini Padmakumar[22], Nicholas Palaskas[22], Jay J. Patel[22], Sabitha Prabhakaran[22], Lucas Ramsey[22], Vinod Ravi[22], Cristhiam Rojas Hernandez[22], Bilja Sajith[22], Paul A. Scheet[22], Stephanie Schmidt[22], Kenna R. Shaw[22], Sanjay Shete[22], Daniel P. Shoenthal[22], Lessley J. Stoltenberg[22], Hussein Tawbi[22], Anastasia Turin[22], Samir Unni[22], Benju Vicknamparampil[22], Max C. Weber[22], John Weinstein[22], Scott Eric Woodman[22], Mark C. Wozny[22], Carol Wu[22], Jia Wu[22], James C. Yao[22], Chingyi Young[22], Emily Yu[22], Steven Zatorski[22], Thomas A. Aloia[23], John Cuenca Trujillo[24], Christopher Gibbons[25], Anai Kothari[26], Ishwaria Subbiah[27] & Phillip Thompson[28,29]

[22]The University of Texas MD Anderson Cancer Center, Houston, TX, USA. [23]Ascension, St Louis, MO, USA. [24]University Health, San Antonio, TX, USA. [25]Oracle Health, Kansas City, MO, USA. [26]Department of Surgery, Medical College of Wisconsin, Milwaukee, WI, USA. [27]Cancer Care Equity and Professional Wellness, Sarah Cannon Research Institute (SCRI), Nashville, TN, USA. [28]Sir Peter MacCallum Cancer Centre, Melbourne, Victoria, Australia. [29]Monash Institute of Pharmaceutical Sciences, Monash University, Parkville, Victoria, Australia.

Methods

Retrospective studies

We completed a non-interventional, retrospective review of patient data using the MDACC electronic health record system, which contains a record of the patients who are treated at the primary campus of MDACC, a large quaternary cancer hospital in Houston, Texas. The chart review for this study involved three groups of patients: (1) patients with tumour biopsies confirming stage III or stage IV NSCLC between January 2017 and September 2022; (2) patients with melanoma of any stage who received single- or multi-agent immune checkpoint blockade between January 2019 and December 2022; and (3) a tissue-agnostic cohort, which included all patients with pathology results for PD-L1 from January 2020 to October 2023 at our institution across a wide range of histologies. This study was approved by the MD Anderson Cancer Center institutional review board. Informed consent was waived due to the retrospective and de-identified nature of the data. The data-collection cut-off was 1 September 2024; data analysis was performed from 1 September 2024 to 29 July 2025.

In the NSCLC dataset, patient information was collected regarding patient demographics (such as age at immunotherapy start, sex, ethnicity), primary tumour histology, clinical stage, known tumour mutations (such as those in EGFR, KRAS, HER2, ALK, MET, p53 and RET), metastatic burden at immunotherapy start (brain, liver), Eastern Cooperative Oncology Group (ECOG) performance status (PS; range, 0–5) near the initiation of immunotherapy, radiation therapy in the time around immunotherapy start, chemotherapy history, immunodeficiency, comorbidities (heart disease, kidney disease, liver disease, respiratory disease), history of other primary tumours, steroid use around immunotherapy initiation, date of last follow-up, date of death, date of first recurrence or progression, ICI agent names and start dates, COVID-19, influenza and pneumococcal vaccination dates, and TPS. Recorded PD-L1 expression as reported below was required for inclusion in the survival analysis for NSCLC. For patients with multiple biopsies, the PD-L1 expression recorded from the closest biopsy to ICI start was used for analysis.

In the melanoma dataset, patient information was collected regarding patient demographics (including age at immunotherapy start, sex, ethnicity), primary tumour histology, clinical stage, known tumour mutations (such as those in EGFR, KRAS, HER2, ALK, MET, p53 and RET), metastatic burden at immunotherapy start (for example, brain, liver), PS (range, 0–5) at the initiation of immunotherapy, chemotherapy history, immunodeficiency, comorbidities (for example, heart disease, kidney disease, liver disease, respiratory disease), other primary tumour data, steroid use around COVID-19 vaccination and immunotherapy initiation, date of last follow-up, date of death, date of first recurrence/progression, ICI agent names and start dates, and COVID-19 vaccination dates. Although our dataset did not include specific vaccine formulations administered to each patient, vaccine formulations administered during the study period included the original monovalent mRNA-1273 vaccine from Moderna (100 μg mRNA prime, 50 μg mRNA booster) released on 18 December 2020; the bivalent Moderna vaccine targeting the original strain and Omicron BA.4/BA.5 (50 μg mRNA) released on 1 September 2022; the original monovalent vaccine from Pfizer/BioNTech (30 μg mRNA prime and booster) released on 11 December 2020; and the Pfizer/BioNTech bivalent formulation (30 μg mRNA) released on 31 August 2022.

Patients were separated into two groups: (1) patients who received a COVID-19 mRNA vaccination within 100 days of ICI start; and (2) patients who did not receive a COVID-19 vaccination. Survival analysis was performed using these groups, with subanalysis involving staging of the tumour, brand of mRNA vaccine, number of doses of the COVID-19 vaccine, location of metastases and cycle of immunotherapy.

For patients who received COVID-19 mRNA vaccination in both the NSCLC and melanoma datasets, OS was calculated as the time between the date of immunotherapy start closest to the mRNA vaccination date, and the last follow-up date or date of death. For patients who did not receive COVID-19 mRNA vaccination, OS was calculated as the time between the initiation of their first ICI start and the date of death or last follow-up. For patients who received COVID-19 mRNA vaccination, PFS was calculated as the time between the initiation of ICI closest to mRNA vaccination and the first incidence of either pathology-confirmed recurrence or imaging-confirmed progression, whichever occurred earlier, that was declared progression in their primary medical oncologist's clinical notes. For patients who did not receive COVID-19 mRNA vaccination, PFS was calculated as the time between their first ICI start date and clinician-confirmed progression as described above. Patients who progressed before the receipt of mRNA vaccination were included in the vaccination group for this analysis. Kaplan–Meier curves were generated using GraphPad Prism.

Cox proportional hazards regression

For Cox proportional hazards regression, time-dependent variables were defined as described in the figure captions. Continuous/numbered variables (such as age, BMI, PD-L1 expression, ECOG and treatment year) were retained as numeric. Binary and categorical variables (for example, stage, gender, mutational status, comorbidities) were converted into factors. For each variable, we constructed individual Cox proportional hazards models. HRs, 95% CIs (Wald) and P values were extracted from model summaries. Variables with $P < 0.05$ in univariable analysis were considered for multivariable modelling. Multivariable Cox proportional hazard regressions were similarly generated with significant variables from univariable analysis. For multivariable Cox proportional hazards regressions, patients with missing values were excluded from analyses.

Categories with fewer than five cases are reported for completeness but were considered not statistically meaningful due to convergence and insufficient data for reliable inference. Variables with significant relationships with survival were included in multivariable analyses (MVAs), and those significant after MVA ($P < 0.05$) were included in PSM. Certain variables (for example, steroid use within 1 month of vaccine) represented subgroups of the treatment cohort by definition. These were evaluated descriptively and in univariable models but were not included as covariables in MVAs, as they do not represent baseline confounders and were not significant on univariable analysis.

We assessed the proportional hazards assumption in multivariate models by evaluating Schoenfeld residuals and found no major violations.

Imputation and PSM

A small number of patients in the NSCLC dataset did not have documented ECOG scores, which were an important predictor of outcomes in Cox proportional hazards regression. BMI had missingness in initial univariable analyses but, because it was not required for PSM, imputation was not performed to address the missingness. Multivariable logistic regression and ridge regression were used to evaluate associations between ECOG missingness and clinically relevant pretreatment covariables. Ridge regression was selected due to multicollinearity between important variables that could not be excluded from the model. Variables not included in models predicting ECOG missingness were vaccination status, steroid usage within a timeframe of vaccination or ICI, PD-L1, concurrent chemotherapy, immunotherapy agent and BMI (as mentioned above). Subsequent ridge regression analysis suggested that ECOG scores in this analysis had a high probability of exhibiting missingness at random.

Given the small sample size in the stage III NSCLC dataset treatment group, multiple imputation was performed to estimate missing ECOG values using chained equations and the R package MICE, where predictive mean matching (PMM) (with set.seed(2025)) was used to create five imputed datasets. Variables used for imputation were chosen based

on large absolute ridge regression coefficients ($|\beta| > 0.3$) and clinical relevance to ensure that prediction of ECOG missingness occurred with accuracy. After selection using regression coefficients, age and previous cycles of systemic therapy were included due to clinical importance. To facilitate PSM while maintaining power in patients with stage III NSCLC, the mode of the five imputed ECOG values was used as a single value for each patient ($n = 5$). This approach was necessary to minimize variance inflation and avoid diluting treatment effects in a very small sample. As PMM is random, small deviations in variable definition, factor levels and row ordering may result in slightly different imputed values. However, sensitivity analyses with slightly different mode selection in the case of ties, different seeds and an increased number of datasets ($n = 20$ or $n = 10$ rather than $n = 5$) revealed similar outcomes ($P < 0.05$) after subsequent matching. The plausibility of imputed values was assessed using density plots, which demonstrated appropriate range and overlap between observed and imputed ECOG values.

After imputation, PSM was performed using the R MatchIt package. A logistic regression model was used to estimate propensity scores, predicting treatment assignment of 'vaccine within 100 days' or 'no vaccine' with covariables based on significant factors associated with survival from MVA, including original or imputed ECOG scores. Across all propensity score analyses, nearest-neighbour matching was performed on the previously estimated propensity scores to identify a balanced cohort. In the case of stage III unresectable NSCLC PSM, nearest-neighbour PSM was performed with a caliper of 0.1 and a 2:1 ratio of control patients to treated patients in stage III UR NSCLC to improve covariable balance and maximize statistical power. Sensitivity analysis with removal of ECOG from the PSM model revealed similar trends.

In stage IV NSCLC, patients with missing ECOG were excluded due to sufficient remaining sample size. PSM was once again performed with nearest-neighbour matching, with a caliper of 0.1 and a 1:1 ratio of control patients to treated patients. Sensitivity analyses with removal of ECOG from PSM rather than imputation and with the same methods as reported in stage III NSCLC (with the same caliper of 0.1 but with a ratio of 1:1 rather than 2:1) also each revealed statistically significant results.

No imputation was performed in the melanoma cohort due to completeness of variables. The melanoma PSM analyses were run with nearest-neighbour matching with a caliper of 0.1 and a 1:1 ratio of control patients to treated patients.

Across all matched cohorts, absolute standardized mean differences (|SMD|) of pscores were consistently less than 0.05 after matching, indicating excellent balance between groups. Balance diagnostics were confirmed visually using jitter plots and histograms of propensity scores.

Survival analysis

The Kaplan–Meier method was used to estimate survival distributions for the matched groups. Log-rank tests were conducted to assess the differences between treatment groups. GraphPad Prism was used to visualize Kaplan–Meier curves, 95% CIs and at-risk numbers at 0, 10, 20, 30 and 40 months, including after extraction of propensity score-matched data from R. Comparisons between groups in primary datasets (Fig. 1) were reported as adjusted HRs calculated with Cox proportional hazard regression. Comparisons between groups in subgroup analyses were reported as unadjusted HRs calculated with log-rank tests to preserve robustness. *P* values are reported for primary survival analyses.

In settings in which Kaplan–Meier curves crossed, the restricted mean survival time was calculated using area under the curve analysis of the absolute differences between arms at 12 and 24 months.

All statistical analyses were conducted in R v.4.4.2 (2024-10-31) and GraphPad Prism.

Quantification of PD-L1 expression in biopsy samples

For patients in both the tissue-agnostic cohort and the NSCLC dataset, biopsy date, pathology reports, histological information and diagnosis codes were collected for patients who had received a biopsy with pathology evaluating PD-L1 at MD Anderson (from January 2020 to October 2023 for the tissue-agnostic cohort and August 2016 to August 2022 for the NSCLC cohort). PD-L1 on tumour cells (TPS) and PD-L1 on tumour cells and immune cells together (CPS) were obtained from pathology reports. Data were curated according to the following principles: (1) simple quantitative values were replicated exactly; (2) TPS values of "<1%" were reported as 0%; (3) for patients with a CPS of 0% or CPS <1% with no TPS value, TPS was reported as 0%, as CPS of 0 or <1% implies a lack of expression of PD-L1 on both tumour cells and myeloid cells; (4) TPS values between 1.1 and 49.9 reported as "<*x*%" or ">*x*%" were excluded due to lack of interpretability; (5) TPS values of >50% were recorded as 50% and TPS values >60% were recorded as 60%, and so on, as these values indicate high PD-L1 expression. For ranges of PD-L1 expression (for example, 0–5%), the median of the numbers in the range was taken as an approximate estimation of PD-L1 on tumours. Replicate patient biopsies (repeat biopsies performed on the same patient within 2 months of a previous biopsy) were excluded, and the earliest biopsy was included.

Separately, survival was analysed in the tumour-agnostic dataset with any COVID-19 mRNA vaccine within 100 days of ICI compared with patients who had no recorded history of a COVID-19 vaccine. Survival analysis was performed as listed in the NSCLC dataset for all patients in this dataset who were treated with ICI in this cohort. TPS values were not required for inclusion.

For group-wise analysis, patients in these cohorts were grouped into (1) those who received their closest COVID-19 mRNA vaccination less than 100 days before tissue biopsy; (2) patients who received their closest COVID-19 mRNA vaccine more than or exactly 100 days before tissue biopsy; and (3) patients who did not receive a COVID-19 mRNA vaccination before biopsy. Patients who received non-mRNA-based COVID-19 vaccines within 100 days before biopsy were included in the no-vaccine group.

Healthy human participants

Studies in healthy volunteers were approved by the MD Anderson Institutional Review Board. Informed consent was obtained from each healthy participant before plasma and peripheral blood mononuclear cells were collected and stored at baseline, 6 h, 24 h and 48 h, or baseline, 6 h, 24 h, 7 days and 14 days after COVID-19 mRNA vaccination, depending on the formulation used. BNT162b2 (COVID-19 mRNA vaccine, 2024–2025 formula, with 30 µg mRNA) and mRNA-1273 (Spikevax Monovalent XBB.1.5, COVID-19 mRNA vaccine, 2023–2024 formulation, with 50 µg mRNA) were used for the first and second timeframes, respectively. Frozen plasma was thawed and analysed using the NULISAseq Inflammation Panel 250 by Alamar Biosciences. Absolute quantification of IFNα concentrations was performed using the NULISAseq Inflammation Panel AQ. Statistical analysis was performed using R, in which we evaluated significance using a linear model with fixed effects based on the time from vaccine and controlling for patient ID (paired), including accommodation of biological variance between the baselines using the limma package's duplicateCorrelation function. *P* values were calculated using moderated *t*-tests with FDR correction for multiple testing. For comparisons between Pfizer and Moderna vaccines, we used a linear modelling approach (limma) to assess the $\log_2$-transformed fold change in cytokine concentrations per-patient from the baseline to 6 h and 24 h. Moderated *t*-tests with empirical Bayes shrinkage were applied, and *P* values were corrected using the Benjamini–Hochberg FDR method. Contrasts were constructed to directly compare Moderna versus Pfizer for each timepoint. Cytokines were visualized if they demonstrated significant differences between Moderna and Pfizer from the baseline to 6 h or 24 h (absolute value of $\log_2$-transformed fold change greater than 0.5 and FDR-corrected $P < 0.05$). Mean expression values per condition were normalized to the baseline and visualized. Volcano plots were generated using R.

Heat maps and graphs of cytokines with significant changes in relative expression in the plasma at 24 h were generated in GraphPad Prism.

Human flow cytometry

Peripheral blood mononuclear cells were thawed in a 37 °C water bath and immediately transferred into a 50 ml tube containing 9 ml of complete RPMI medium (RPMI + 10% FBS) at a ratio of 1 part cells to 9 parts medium. Cells were centrifuged at 400*g* for 10 min, and the supernatant was decanted. The cell pellet was resuspended in 1 ml of PBS, and incubated with live/dead marker (1 µl per 1,000 µl of cell suspension, containing 1–10 million cells per ml) for 30 min at 4 °C. After incubation, 3 ml of PBS + 2% FBS was added, and the cells were centrifuged again at 400*g* for 8 min and the supernatant was decanted. Cells were then pre-incubated with 5 µl of Human TruStain FcX (BioLegend, 422302) per 100 µl of cell suspension for 5 min at room temperature. The cells were then washed with PBS and centrifuged at 400*g* for 6 min. After decanting the supernatant, 10 µl of Brilliant buffer was added to each tube, and the mixture was allowed to sit for 5 min before addition of antibodies targeting extracellular markers and the cells were incubated for 20 min at room temperature in the dark. After incubation, cells were washed and fixed in the dark for 45 min at 4 °C with 500 µl of fixation solution (BD). Cells were then permeabilized with 2 ml permeabilization buffer. Intracellular stains were added in permeabilization buffer, and cells were incubated for approximately 40 min at room temperature. After incubation, cells were washed with permeabilization buffer and resuspended in 200 µl of PBS + 2% FBS. Analysis was then conducted using Cytek Aurora Spectral Flow Cytometer.

Preclinical experiments

All mouse experiments and procedures were approved by the University of Florida or the University of Texas MD Anderson Institutional Animal Care and Use Committee (IACUC). Mice (aged 4–10 weeks) were maintained at 21 ± 1 °C and 35% humidity under a 14 h–10 h light–dark cycle. Mice were randomized prior to treatment. Tumour measurements were performed blinded to the treatment group. Euthanasia was performed by CO_2 inhalation followed by cervical dislocation in accordance with approved protocols. Humane end points included tumour ulceration.

C57BL/6 and *Rigi*-knockout mice (*C57BL/6NJ-Rigiem1(IMPC)J/Mmjax*) were purchased from The Jackson Laboratory (046070-JAX) and bred in house. Tumour-bearing mice were implanted s.c. with 50,000 B16F0 melanoma cells, 1 million B16F10-OVA melanoma cells or 200,000 LLC cells in the right flank. Orthotopic LLC models were implemented by implanting 100,000 LLC cells into the left lung of C57BL6 mice through direct injection below the 9th rib. A mix of male and female mice was used for experiments with B16F0, and male mice were used for experiments with LLC. All mice were vaccinated intramuscularly with 25 µg per dose of RNA-LNP or RNA-LPA (mRNA fraction)[12]. We administered anti-mouse IFNα receptor (aIFNAR1, Bio X Cell, BE0241) and anti-mouse IL-1R (Bio X Cell, BE0256) antibodies intraperitoneally at an initial dose of 500 µg per mouse for the first dose, followed by a maintenance dose of 250 µg per mouse twice a week for the remaining treatment period. Anti-PD-L1 (Bio X Cell, BE0101) checkpoint inhibitor was administered at 400 µg per mouse for the initial dose, followed by a maintenance dose of 200 µg per mouse twice a week for the remaining treatment period. Anti-PD-1 (Bio X Cell, BE0146) checkpoint inhibitor was administered at an initial dose of 400 µg per mouse, followed by a maintenance dose of 200 µg per mouse. LMW poly(I:C) (InvivoGen, tlrl-picw) was administered intramuscularly with 25 µg per mice for two doses. Tumours were measured at a frequency of three times a week starting on day 8 until more than 20% of mice reached the end point. Mice were euthanized after reaching the humane end point.

mRNA

SARS-CoV-2 spike coding sequence with K986P and V987P mutations was inserted into a pGEM-4Z backbone downstream of the T7 promoter with previously published UTRs and poly(A) signal analogous to the mRNA in BNT162b2[30,31]. The 5′ SpeI restriction site was removed from the sequence to allow for restriction of the poly(A) tail. The T7 promoter was changed to have an AGG initiator sequence by site-directed mutagenesis (NEB, E0554) according to the company's recommended protocol. Plasmids were grown in NEB5a competent *Escherichia coli* and purified using the RNeasy Maxi kit (Qiagen, 75162) and sequenced using whole-plasmid sequencing by Genewiz. Plasmids were restricted by using 2 U µg^{-1} SpeI HF (NEB, R3133L) for 2 h at 37 °C followed by DNA precipitation. mRNA was synthesized using the mMESSAGE mMACHINE T7 mRNA Kit with CleanCap Reagent AG (Thermo Fisher Scientific, A57620). Spike mRNA was made using CleanCap reagent AG (3′ OMe) (Trilink, N-7413-5) and N^1-methylpseudouridine-5′-triphosphate (Trilink, N-1081-10). PP65 mRNA was capped using ARCA (NEB, S1411L) followed by treatment with mRNA cap 2′-*O*-methyltransferase (NEB, M0366L). The in vitro transcription reaction was performed at 20 °C for 10 h. DNA was removed according to the kit instructions and RNA was purified using the RNeasy maxi kit (Qiagen, 75162). RNA was eluted in purified RNase-free water and stored at −80°C until use. mRNA was checked for quality using an Agilent TapeStation 4150. After thawing, RNA was diluted to 100 µg ml^{-1} in RNase-free water followed by incubation at room temperature or 72 °C for 3 min. Then 100 ng of RNA or 1 µl of ladder was added to 5 µl of RNA ScreenTape sample buffer (Agilent, 5067-5577) and mixed at 2,000 rpm for 1 min. The samples were run using an RNA ScreenTape (Agilent, 5067-5576). For dsRNA removal, the method described previously was followed[20]. In brief, mRNA was precipitated and reconstituted in chromatography buffer. Cellulose fibres (Sigma-Aldrich, C6288-100G) suspended in chromatography buffer were added to Nucleospin filter units (Macherey-Nagel, 740606) followed by washing. Up to 500 µg of RNA per filter unit was added to cellulose and incubated by rapid mixing for 30 min. RNA was recovered by centrifugation, and incubation was repeated using a second column containing cellulose fibres. RNA was then filtered through a 0.45 µm syringe filter (Pall, 4604) to remove any cellulose particulate before being precipitated and reconstituted in RNase-free water[20].

Fabrication of LNPs

Before complexation, 0.5 M of RNase-free citrate buffer (pH 3.75) (Teknova, Custom order) was added to the RNA for a final concentration of 0.1 M. ALC-0159 (Avanti, 880155 P), ALC-0315 (Avanti, 890900 O), cholesterol (Sigma-Aldrich, C8667) and DSPC (Avanti, 850365P) were reconstituted in 100% ethanol at a ratio of 1.7:47.5:40.8:10. Lipids and RNA were mixed at a 3:1 FRR on a Nanonsemblr Ignite (Precision NanoSystems, now part of Cytiva) for an N/P ratio of 6. RNA-LNPs were dialysed overnight at 4 °C with two buffer exchanges at the 3 h and 6 h timepoints using a 3.5 kDa dialysis cassette (Thermo Fisher Scientific, A52967). After dialysis, LNPs were filtered through the 0.2 µM Supor EX ECV filter (Pall, KS2ECV2S). LNPs were concentrated using 30 kDa Amicon filters (Millipore, UFC903024) by centrifugation at 2,000*g*. The final LNP formulation had sucrose dissolved in PBS added for a final concentration of 12%. Anionic RNA-LPAs were made as previously described[12]. In brief, DOTAP liposomes 2.5 mg ml^{-1} were mixed with mRNA at a 1:1 mass to mass ratio and complexed for 15 min at room temperature before administration.

RNA concentration was determined in LNPs using the RiboGreen assay (Invitrogen, R11490) using the BioTek Cytation 3 plate reader. The encapsulation efficiency was determined by comparing readings to LNPs in TE buffer versus LNPs in 1% Triton X-100. LNPs were diluted up to 500 µg ml^{-1} with PBS before injection. Empty LNPs were used at a volume consistent with the dose of RNA-LNPs fabricated using the same steps and same amounts of lipids. Fluorescence values were plotted in a standard curve with an extrapolation factor set to 1.1. The values from wells with Triton X-100 (total mRNA) and TE buffer (free mRNA) was entered into the following equation: EE% = [1 − (Free RNA/Total RNA)] × 100%. Total mRNA RNA-LNPs were also loaded onto a 1%

agarose gel made in 1× TAE buffer (Quality Biological, 351-008-131) with GelRed (Biotium, 41003-T). Then 500 ng of RNA was loaded into LNPs and free RNA was mixed with 6× SDS-free (NEB, B7025S) loading dye and run at 90 V for 45 min. Particle size was acquired using a Malvern Zetasizer Ultra and NanoSight's NS300. Before particle-size, PDI, concentration and surface ζ potential analysis, LNPs were diluted 100-fold with HyClone HyPure water (Cytiva, SH30538.02). They were and run in triplicate at 25 °C on the Zetasizer. Orthogonal particle-size distribution and concentration measurements were carried out using Malvern's NanoSight NS300 NTA equipment. Each LNP sample was diluted 500-fold with PBS and pumped through the equipment at constant speed for five captures with optimized camera settings. An optimized detection threshold was set for analysis. mRNA was extracted from LNPs by dissolving 750 μg ml^{-1} with 5 volumes of ethanol or 2 volumes of isopropanol followed by 2 washes with cold 70% ethanol. RNA pellets were dissolved in RNase-free H_2O before analysis using the TapeStation.

Plasma collection

Mice were bled through the retroorbital route using heparinized capillaries (Thermo Fisher Scientific, 22-362566) collecting a maximum of 200 μl into EDTA coated tubes (Thermo Fisher Scientific, NC9414041). Whole blood was centrifuged at 1,200*g* for 15 min. Plasma was collected and stored at −80 °C until use.

Processing tumours for flow cytometry analysis

Tumours were dissected from euthanized mice with the external fibrous sac left intact. Tumours were bisected using a scalpel and half of each sample was placed into a GentleMacs column GentleMACS C Tube (130-096-334) with an enzyme mix containing 10 mg ml^{-1} of collagenase (Sigma-Aldrich, C5138-1G), 1 mg ml^{-1} of hyaluronidase (StemCell Technologies, 07461) and 200 mg ml^{-1} of DNase (Sigma-Aldrich, D5025-150KU) or using the tumour dissociation kit (Miltenyi, 130-096-730) followed by debris removal (Miltenyi, 130-109-398). Samples were run on a m_TDK_1 cycle and centrifuged at 300*g* for 5 min after completion. The pellets were resuspended in cold PBS and filtered through a 70-μm cell strainer. The samples were washed twice using cold PBS and then manually counted using a haemocytometer.

Isolation of splenocytes

Whole spleens were collected from euthanized mice and placed into cold RPMI medium. The spleens were then teased through a 70-μm filter and lysed for 5 min at 37 °C using 1× BD Pharmalyse buffer (BD, 555899). Lysis buffer was quenched with medium and centrifuged at 500*g* for 5 min. Splenocytes were resuspended in cold PBS and filtered through a 70-μm cell strainer and washed once with PBS before being counted using the Beckman Coulter Vi-cell XR or haemocytometer.

Mouse flow cytometry analysis

In total, 1×10^6 cells from either tumours and spleens were placed into 96-well V-bottom plates. Unless stated otherwise, the washing steps were performed by centrifugation at 500*g* for 5 min at 4 °C followed by resuspension of cells with 200 μl of buffer, with mixing done by pipetting. Cells were washed with cold PBS and stained with 100 μl of live/dead stain (Thermo Fisher Scientific, L10119) for 30 min at 4 °C. Live/dead dye was quenched with 100 μl of cold PBS and the cells were washed once with cold FACS buffer (PBS with 2% FBS). Cells were centrifuged and resuspended with 10 μl True stain FCX buffer (BioLegend, 422302) diluted to 100 μg ml^{-1} with FACS buffer for 10 min. Then 90 μl of antibodies (Supplementary Tables 12 and 13) and Brilliant Stain buffer (BD, 563794) were added and incubated for 30 min at 4 °C. Next, 100 μl of FACS buffer was added to each well and the cells were washed twice with cold FACS buffer. Cells were fixed for 15 min with 100 μl of Cytofix buffer (BD, 554655) at 4 °C. Next, 100 μl of PBS was added to each sample and cells were washed twice and stored in FACS buffer at 4 °C in the dark until analysis. Initial compensation was acquired using Ultracomp eBeads (Thermo Fisher Scientific, 01-2222-42) and ArC amine reactive compensation beads (Thermo Fisher Scientific, A10346). Results were acquired using a BD Symphony A3 and analysed using FlowJo v.10.8.1 and v.10.10.0.

Tetramer production

Peptides selected to be high-affinity binders for Survivin (ATFKNWPFL), GP100A (EGSRNQDWL), GP100B (KVPRNQDWL), WT1 (RMFPNAPYL), CLDN6 or claudin 6 (KVYDSLLAL) and TRP2 (SVYDFFVWL) were purchased from GenScript. H2-Db and H2-Kb monomers were purchased as easYmers from ImmunAware (5001-01 and 5004-01, respectively), and tetramers were prepared according to the manufacturer's instructions. In brief, peptides were reconstituted to 1 mg ml^{-1} in deionized water, further diluted to 75 μM and incubated with easYmer (Eagle Biosciences, 5004-01, 5001-01) at 18 °C for 48 h. The resulting complexes were tetramerized by gradually mixing with streptavidin-APC (BD Biosciences, 554067). After incubation, a final stock concentration of 500 nM for each tetramer was achieved.

Tetramer staining

According to the manufacturer recommendations, $1–2 \times 10^6$ cells were stained with tetramer diluted to 20 nM in FACS buffer. Cells were left to stain in the dark at room temperature for 1 h, washed once with FACS buffer, co-stained with surface antibodies (CD3, CD4) at room temperature for 20 min, washed twice with FACS buffer and analysed on a Cytek Aurora flow cytometer.

AIM assay

The AIM assay was performed as previously described[12]. In this iteration, whole splenocytes were used rather than isolated T cells. In brief, 24 h after the last RNA-LNP vaccine, splenocytes were collected for antigen recall assay. Spleens were collected and processed as described above. 1 million splenocytes were cultured in a 96-well round-bottom plate in T cell medium containing RPMI 1640 (Gibco, 11-875-119), 10% FBS (Thermo Fisher Scientific, 35-011-CV), 1% penicillin–streptomycin (Gibco, 30-002-CI), 1% MEM non-essential amino acids (NEAA, Gibco, 11140050), 1% sodium pyruvate (Gibco, 11360070), 0.1% β-mercaptoethanol (BME, Gibco, 21985-023) and 0.2 μg tumour-associated peptides without cytokines. Peptides were chosen based on their suggested upregulation in melanoma tumours[12]. Selected peptides were purchased from JPT Peptide Technologies and reconstituted according to the manufacturer's guidelines. Co-culture was maintained for 48 h in an incubator at 37 °C under 5% CO_2. Cells were next collected and stained for the AIM assay for evaluating activation of antigen-specific T cells. Cells were centrifuged and resuspended in FACS buffer containing antibodies mix (Supplementary Table 14). Cells were washed three times and fixed using fixation medium (Thermo Fisher Scientific, GAS001S100) for 15 min at room temperature. Cells were washed once with PBS and were stored in FACS buffer at 4 °C in the dark until analysis. Results were acquired using a BD Fortessa III. Values were normalized by subtracting the percentage of AIM^+ cells of tbe DMSO-only controls from each treatment condition. Statistical analysis was performed using Brown–Forsythe and Welch ANOVA, followed by Dunnett's T3 multiple-comparison test.

ELISA and multiplex analysis

Plasma was analysed for cytokine concentration using ELISAs and multiplex cytokine arrays. A portion of the plasma samples were assessed for IFNα through ELISA (Invitrogen, BMS6027). Plasma was also sent for analysis by Eve Technologies for multiplex cytokine array (MD44). For quantification of spike IgG, mice that received three vaccines/vehicle doses during tumour studies were bled once the humane end point was reached. Spike-specific IgG was determined using an Anti-mouse SARS-CoV-2 IgG titre assay (AcroBiosystems, RAS-T023). Plasma was diluted 100,000-fold and run according to the company's recommended parameters for semiquantitative analysis.

Immunofluorescence

Half of bisected tumours were fixed with 4% paraformaldehyde at 4 °C overnight. The samples were washed three times using PBS and then immersed successively into 10%, 20% and 30% sucrose for cryopreservation. Tissue was then embedded in O.C.T. (Tissue-Tek, 4583) and stored at −80 °C. Blocks of tissue were moved to −20 °C for 24 h and were sectioned at a thickness of 30 µm using the Leica cryostat, and the sections were placed onto microscope slides. Before staining, the slides were brought up to room temperature for 15 min and washed three times with PBS. Tissue was blocked at room temperature for 1 h using a blocking buffer containing 2% goat or donkey serum, 1% BSA and 0.1% Triton X-100 in PBS. The sections were then stained with primary antibodies (Supplementary Table 15) in blocking buffer overnight at 4 °C. After incubation, the sections were washed three times with PBS and stained with secondary antibodies (Supplementary Table 15) diluted in blocking buffer for 1 h at room temperature. After three 5 min PBS washes, the sections were incubated with DAPI (1:1,000 in PBS) for 10 min at room temperature. After a triple PBS wash, the sections were mounted with Prolong Glass Antifade Mountant (Thermo Fisher Scientific, P36984) and covered with a cover glass. Images were acquired using a Leica Stellaris 8 WLL Spectral Confocal Microscope. Image processing was performed using Fiji ImageJ software (NIH) and Imaris (Oxford Instruments).

Reporting summary

Further information on research design is available in the Nature Portfolio Reporting Summary linked to this article.

Data availability

Data generated in this study are available in the Article and its Supplementary Information. All clinical data are de-identified to protect patient privacy. Source data are provided with this paper.

30. Nance, K. D. & Meier, J. L. Modifications in an emergency: the role of N^1-methylpseudouridine in COVID-19 vaccines. *ACS Cent. Sci.* **7**, 748–756 (2021).
31. Orlandini von Niessen, A. G. et al. Improving mRNA-based therapeutic gene delivery by expression-augmenting 3′ UTRs identified by cellular library screening. *Mol. Ther.* **27**, 824–836 (2019).

Acknowledgements Research reported in this publication was supported by the National Cancer (NCI) Institute under the University of Texas MD Anderson Cancer Center SPORE in Melanoma P50CA221703, the University of Texas MD Anderson Cancer Center Support Grant P30CA016672, T32-CA196561-08 (A.J.G.), R37CA251978 (E.J.S.) and R01CA266857 (E.J.S.). This research was also supported by an FDA orphan disease award R01FD007268 (E.J.S.), foundation grants from the American Brain Tumour Association, the Radiological Society of North America, Conquer Cancer Foundation, the Cullen M. Taniguchi Immuno-Radiotherapy Symposium Seed Award, ASTRO-LUNGevity, Live Like Bella Childhood Cancer Foundation/Florida Department of Health, CureSearch (Catapult Award), Stop Children's Cancer and the Bonnie R. Freeman Professorship, Danny's Dream, Ian's Friend's Foundation, Alex's Lemonade Stand (R Accelerated Award), the Rally Foundation for Childhood Cancer Research, the Medulloblastoma Initiative (MBI) and Cure Group 4 medulloblastoma consortium, The National Pediatric Cancer Foundation and philanthropic contributions to The University of Texas MD Anderson Lung Moon Shot Program. The content is solely the responsibility of the authors and does not necessarily represent the official views of the funding sources including the National Cancer Institute. We thank D. Montgomery, L. Saldarriaga, X. Ma, C. von Roemeling and D. Zhang for their help with animals experiments; D. Li for his help with statistical analysis; and the staff at the Melanoma Informatics, Tissue Resource and Translational Pathology Core (MelCore) and the Flow Cytometry and Cellular Imaging Core Facility at The University of Texas MD Anderson Cancer Center and the ICBR Cytometry Core (RRID: SCR_019119) and animal care facilities at the University of Florida. Images provided in this Article were created using BioRender.

Author contributions A.J.G., S.H.L. and E.J.S. conceived the study, developed the study methodology, directed and supervised all analyses, analysed data, provided resources, acquired funding for the study and wrote the manuscript. C.M. and N.L. conducted, directed, supervised and analysed data for preclinical studies. S.C. conducted, directed, supervised and analysed data for clinical studies. J.-H.L. directed and supervised data analysis. R.S. directed and supervised some data analysis. M.K.R. contributed to overall statistical strategy and data analysis. A.K., E.Y., R. Lohray, E.C., R.K., W.D., R. Liang, J.J., G.G. and N.N. conducted chart review and analysed data for retrospective clinical studies. C.W., M.W., C.B., A.W., S.D.J., D.S., F.W., C.X., E.G., C.Z., A. DeVries, A. Doty, P.C., B.R.S., Y.W., Y.M., J.C., N.C., B.R.S., N.T., G.A. and H.R.M.-G. designed and conducted preclinical studies. A.A., D.A., P.G., K.D. and M.W. assisted in design and execution of translational studies. J.S., A.B.D., X.W., W.R., J. Lewis, J. Lee, A.A.V., D.L.G., H.T., J.Z., J.W., J.V.H and all of the members of the Data-Driven Determinants for Covid-19 Oncology Discovery Effort (D3CODE) Team analysed, aggregated and maintained clinical databases required for retrospective clinical studies. A.J., J.W. and J.V.H. provided guidance regarding retrospective clinical analysis. J.N., B.Y.S.K., P.S. and W.J. interpreted results and developed study methodology. All of the authors contributed to writing, reviewing and editing the final manuscript.

Competing interests A.J.G. has received travel funding from Alamar Biosciences and is a scientific advisor for Sift Biosciences and BeyondSpring Pharmaceuticals. J.Z. reports grants from Merck, grants and personal fees from Johnson & Johnson and Novartis, personal fees from Bristol Myers Squibb, AstraZeneca, GenePlus, Innovent and Hengrui outside the submitted work. D.L.G. is a scientific advisor for AstraZeneca, Eli Lilly, Menarini Richerche, 4D Pharma, Onconova Therapeutics and Sanofi. P.S. is on the scientific advisory committee for Achelois, Affini-T, Akoya Biosciences, Apricity, Asher Bio, BioAtla LLC, Candel Therapeutics, Catalio, C-Reveal Therapeutics, Dragonfly Therapeutics, Earli Inc, Enable Medicine, Henlius/Hengenix, Hummingbird, ImaginAb, InterVenn Biosciences, LAVA Therapeutics, Lytix Biopharma, Marker Therapeutics, Matrisome, Oncolytics, Osteologic, PBM Capital, Phenomic AI, Polaris Pharma, Soley Therapeutics, Spotlight, Trained Therapeutix Discovery, Two Bear Capital and Xilis, Inc., and reports private investments in Adaptive Biotechnologies, BioNTech, JSL Health, Sporos and Time Bioventures. S.H.L. receives grant funding from Beyond Spring Pharmaceuticals and Nektar Therapeutics, serves on the scientific advisory boards for Beyond Spring Pharmaceuticals, AstraZeneca and Creatv Microtech, and is co-founder of and holds stock options in Seek Diagnostics. J.V.H. reports being on advisory committees for BioNTech, Genentech, Mirati Therapeutics, Eli Lilly, Janssen, Boehringer Ingelheim, Regeneron, Takeda, BerGenBio, Jazz, Curio Science, Novartis, AstraZeneca, BioAlta, Sanofi, Spectrum, GlaxoSmithKline, EMD Serono, BluePrint Medicine and Chugai; support from AstraZeneca, Boehringer Ingelheim, Spectrum, Mirati, Bristol Myers Squibb and Takeda; and licensing or royalties from Spectrum. E.J.S. is a paid consultant for Siren Biotechnology, an external advisory board member at Nature's Toolbox (NTX) with stock options, and a scientific advisor for iOncologi, Inc. The Article discusses patented technologies related to RNA therapeutics from A.J.G., C.M., S.H.L, D.S., H.R.M.-G. and E.J.S. Some of these technologies are licensed or under option to license by iOncologi, Inc. H.R.M.-G. and E.J.S. receive royalty payments from patents licensed to iOncologi. The other authors declare no competing interests.

Additional information

Supplementary information The online version contains supplementary material available at https://doi.org/10.1038/s41586-025-09655-y.

Correspondence and requests for materials should be addressed to Adam J. Grippin, Elias J. Sayour or Steven H. Lin.

Peer review information *Nature* thanks Mariano Provencio, Siri Tahtinen and the other, anonymous, reviewer(s) for their contribution to the peer review of this work.

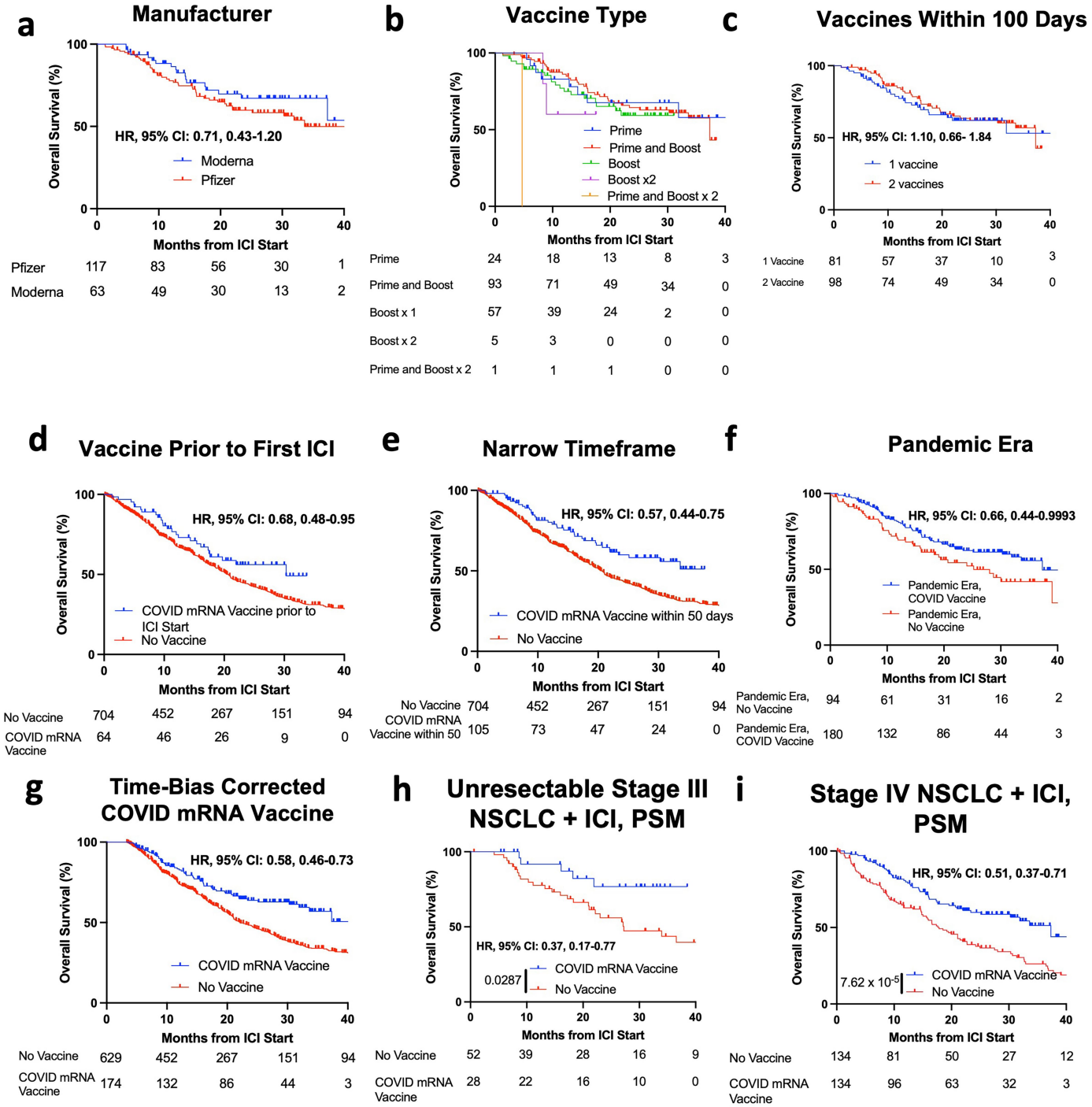

Extended Data Fig. 1 | COVID mRNA Vaccines are associated with improved survival in NSCLC patients who receive ICI. a-c, Overall survival for NSCLC patients who received immune therapy and obtained a COVID mRNA vaccine differentiated by vaccine manufacturer (**a**), whether the patient received their first vaccine during this period ("Prime only"), a booster ("Boost only"), or both a priming vaccine and a booster vaccine within the 100-day period ("Prime and Boost") (**b**), and number of vaccines received within 100 days of ICI initiation **(c)**. One patient who received 3 vaccines within 100 days is not represented. **d**, Overall survival among patients with NSCLC receiving their first round of ICI, stratified by receipt of COVID mRNA vaccine in the 100 days prior to ICI initiation. **e**, Overall survival for NSCLC patients who received immune therapy and obtained a COVID mRNA vaccine within 50 days of initiating immunotherapy. **f**, Overall survival for NSCLC patients receiving ICI starting on or after 9/2/2020, stratified by receipt of COVID mRNA vaccination within 100 days surrounding ICI initiation. **g**, Overall survival for NSCLC patients stratified by receipt of COVID mRNA vaccines with all events occurring in the first 100 days after initiating ICI removed to correct for immortal time bias. **h-i**, Propensity score matching for overall survival in patients with Stage III Unresectable NSCLC (**h**) and metastatic NSCLC (**i**) treated with ICI who received a COVID mRNA vaccine within 100 days of initiating ICI or did not receive a COVID mRNA vaccine. Hazard ratios and p values were calculated by log-rank (Mantel-Cox, two-sided) tests.

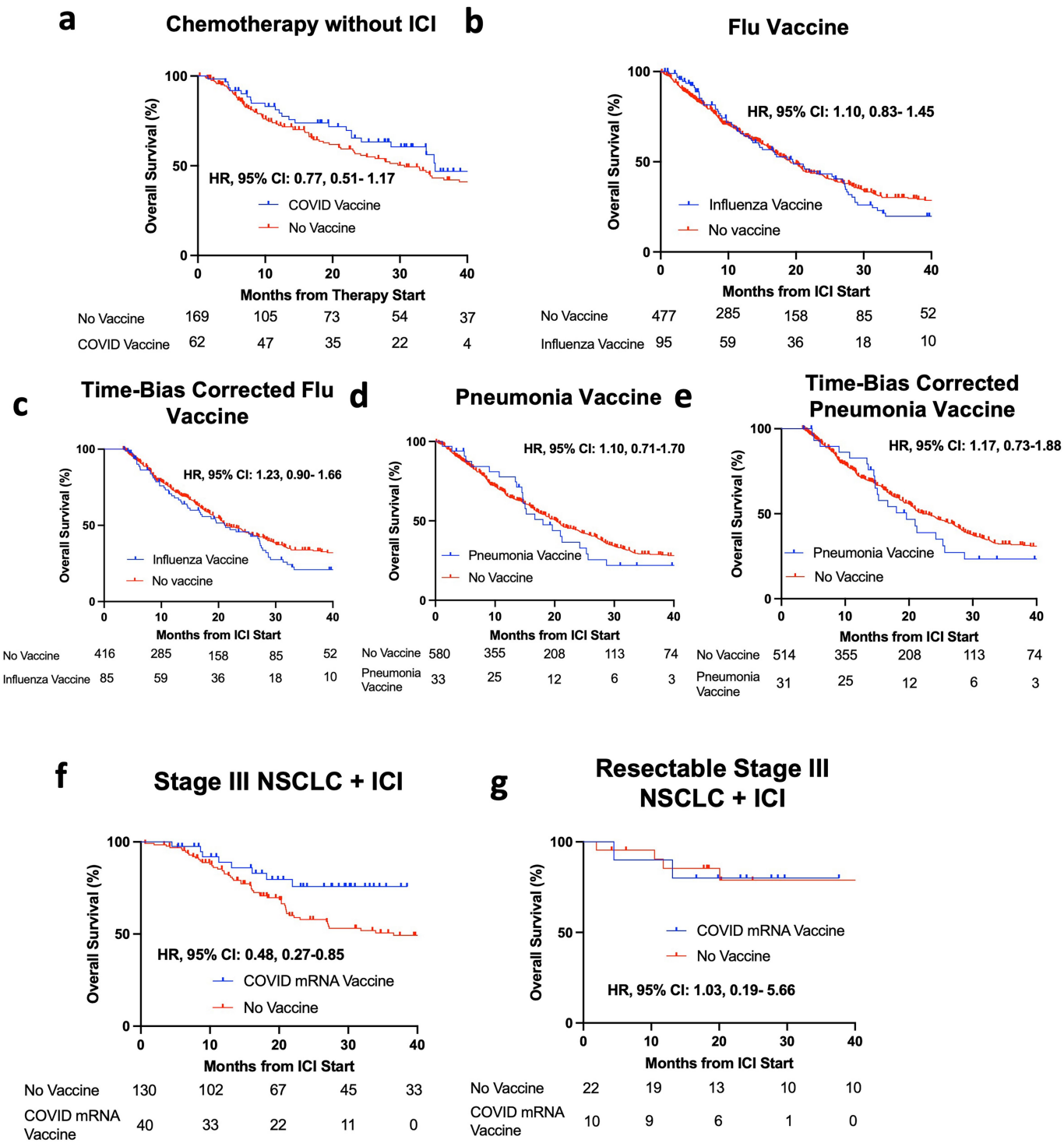

Extended Data Fig. 2 | COVID mRNA vaccines are uniquely associated with improved survival in patients with NSCLC treated with ICI. a, Overall survival for NSCLC patients who did not receive immune checkpoint inhibition and received a COVID vaccine within 100 days of initiating chemotherapy or did not receive a COVID vaccine. **b-e**, Overall survival for NSCLC patients stratified by receipt of influenza vaccines (**b-c**), or pneumonia vaccines (**d-e**) with all events included (**b, d**) or, to correct for immortal time bias, including only events that occured greater than 100 days after initiating ICI (**c, e**). Patients who also received COVID vaccination were excluded from the influenza and pneumonia vaccine analyses. **f-g**, Overall survival for **(f)** all patients with Stage III NSCLC and **(g)** patients with Resectable Stage III NSCLC treated with ICI who received a COVID mRNA vaccine within 100 days of initiating ICI or did not receive a COVID mRNA vaccine. Hazard ratios and p values were calculated by log-rank (Mantel-Cox, two-sided) tests.

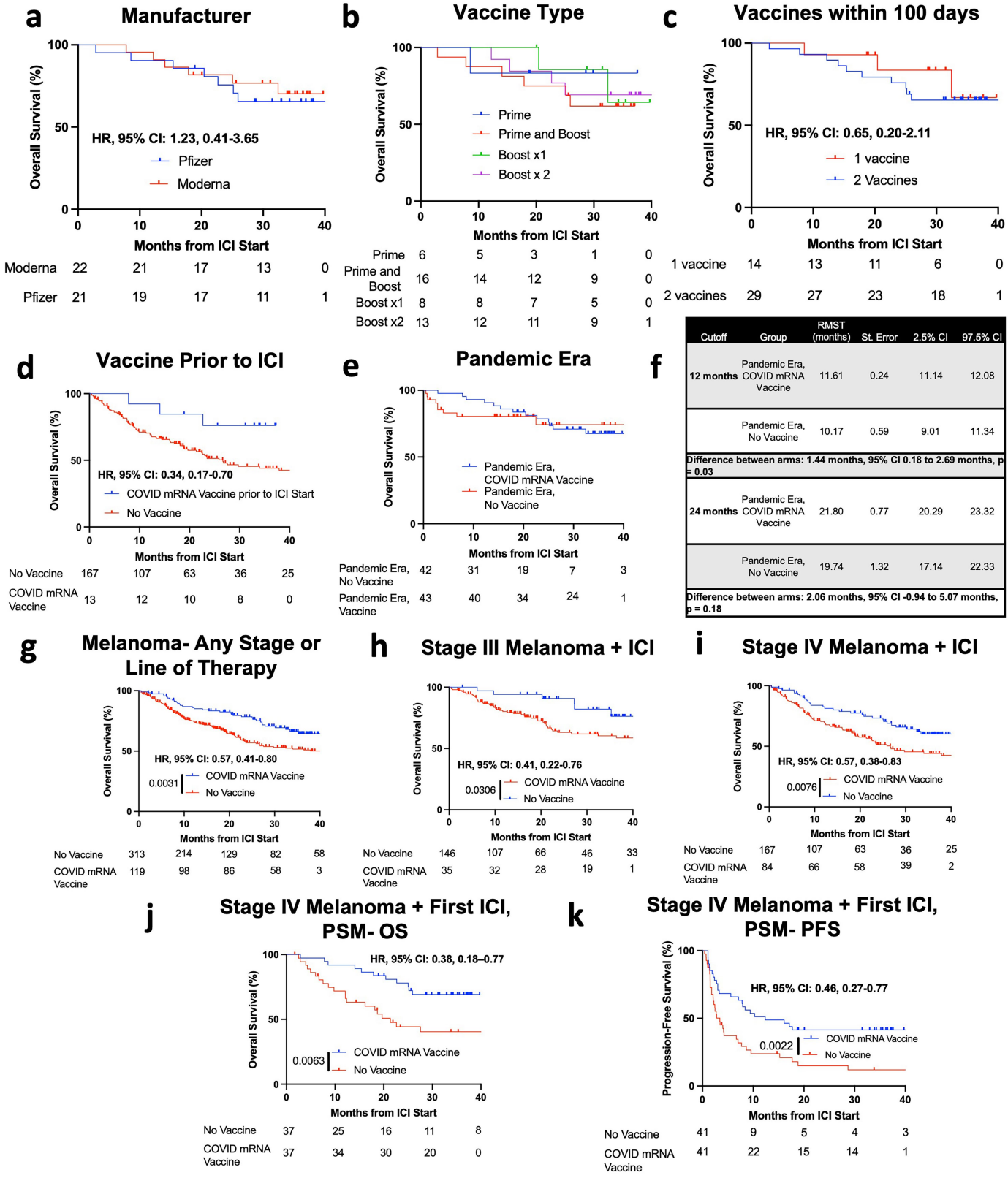

Extended Data Fig. 3 | See next page for caption.

Extended Data Fig. 3 | COVID mRNA Vaccines are uniquely associated with improved survival in melanoma patients who are receiving their first round of ICI. a-c, Overall survival for Stage IV melanoma patients who received their first round of immune therapy and obtained a COVID mRNA vaccine differentiated by vaccine manufacturer (**a**), whether the patient received their first vaccine during this period ("Prime only"), a booster ("Boost only"), or both a priming vaccine and a booster vaccine within the 100-day period ("Prime and Boost") (**b**), and the number of vaccines received within 100 days of ICI initiation (**c**). **d**, Overall survival among patients with Stage IV melanoma who are receiving their first round of ICI stratified by receipt of COVID mRNA vaccine in the 100 days prior to ICI initiation. Hazard ratios are reported using log-rank tests. **e-f**, Overall survival for Stage IV Melanoma receiving ICI starting on or after 9/2/2020, stratified by receipt of COVID mRNA vaccination within 100 days surrounding ICI initiation. For crossing survival curves as in **e**, RMST was calculated rather than logrank (Mantel-Cox) testing (see Methods). **f**, Restricted Mean Survival Time (RMST) at 12 and 24 months. Absolute differences between arms are compared with a two-tailed non-parametric area under the curve (AUC) analysis. **g-i**, Overall survival for patients in the Melanoma dataset treated with ICI. **g**, Survival for patients in the Melanoma cohort treated with ICI who received a COVID mRNA vaccine within 100 days of initiating any line of ICI or did not receive a COVID mRNA vaccine. **h**, Survival for Stage III patients in the Melanoma cohort treated with ICI who received a COVID mRNA vaccine within 100 days of initiating any line of ICI or did not receive a COVID mRNA vaccine. **i**, Survival for all Stage IV patients in the Melanoma cohort treated with ICI who received a COVID mRNA vaccine within 100 days of initiating any line of ICI or did not receive a COVID mRNA vaccine. **j-k**, Propensity score matching for overall survival (**j**) and progression-free survival (**k**) in patients with metastatic melanoma treated with ICI who received a COVID mRNA vaccine within 100 days of initiating ICI or did not receive a COVID mRNA vaccine. Matching was performed using all variables significantly associated with survival on multivariable analysis. Hazard ratios and p values were calculated by log-rank (Mantel-Cox, two-sided) tests unless otherwise specified. Numbers underneath the graph indicate the number of patients at each timepoint.

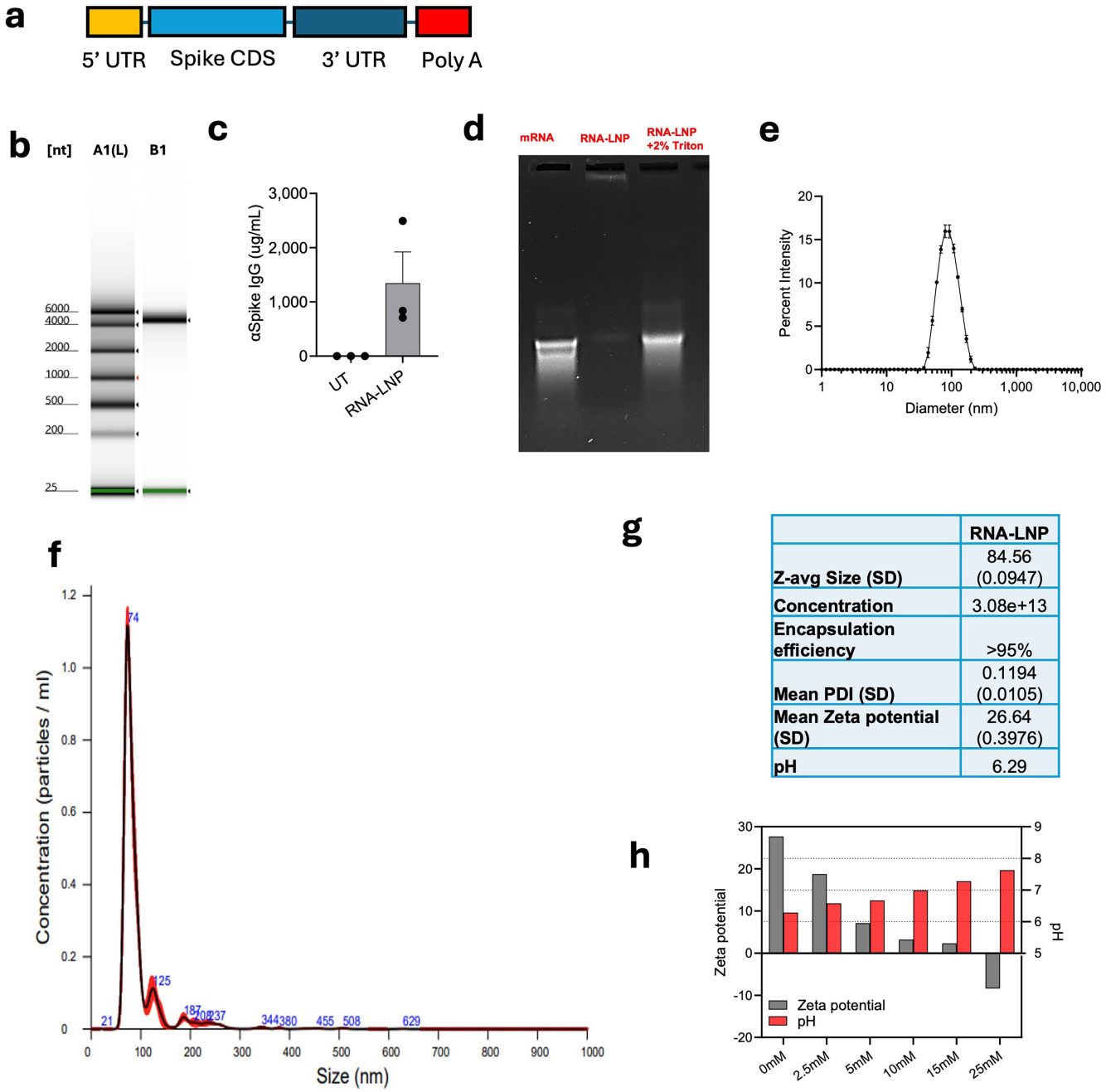

	RNA-LNP
Z-avg Size (SD)	84.56 (0.0947)
Concentration	3.08e+13
Encapsulation efficiency	>95%
Mean PDI (SD)	0.1194 (0.0105)
Mean Zeta potential (SD)	26.64 (0.3976)
pH	6.29

Extended Data Fig. 4 | Synthesis and characterization of RNA-LNPs approximating BNT162b2. a, Sequence map of mRNA. **b**, Quality of mRNA assessed on a BioAnalyzer. **c**, Total anti-Spike IgG generated by C57Bl/6 mice after 3 doses of vaccine (n = 3 biological replicates). Data are displayed as mean with SEM. **d**, Visualization of mRNA loading in LNPs via gel electrophoresis. **e**, Size distribution of LNPs assessed by DLS with 3 technical replicates. Data are displayed as mean with SD. **f**, Size distribution determined via nanoparticle tracking analysis. **g**, Table of LNP properties. **h**, pH and zeta potential at biologically relevant levels of sodium bicarbonate.

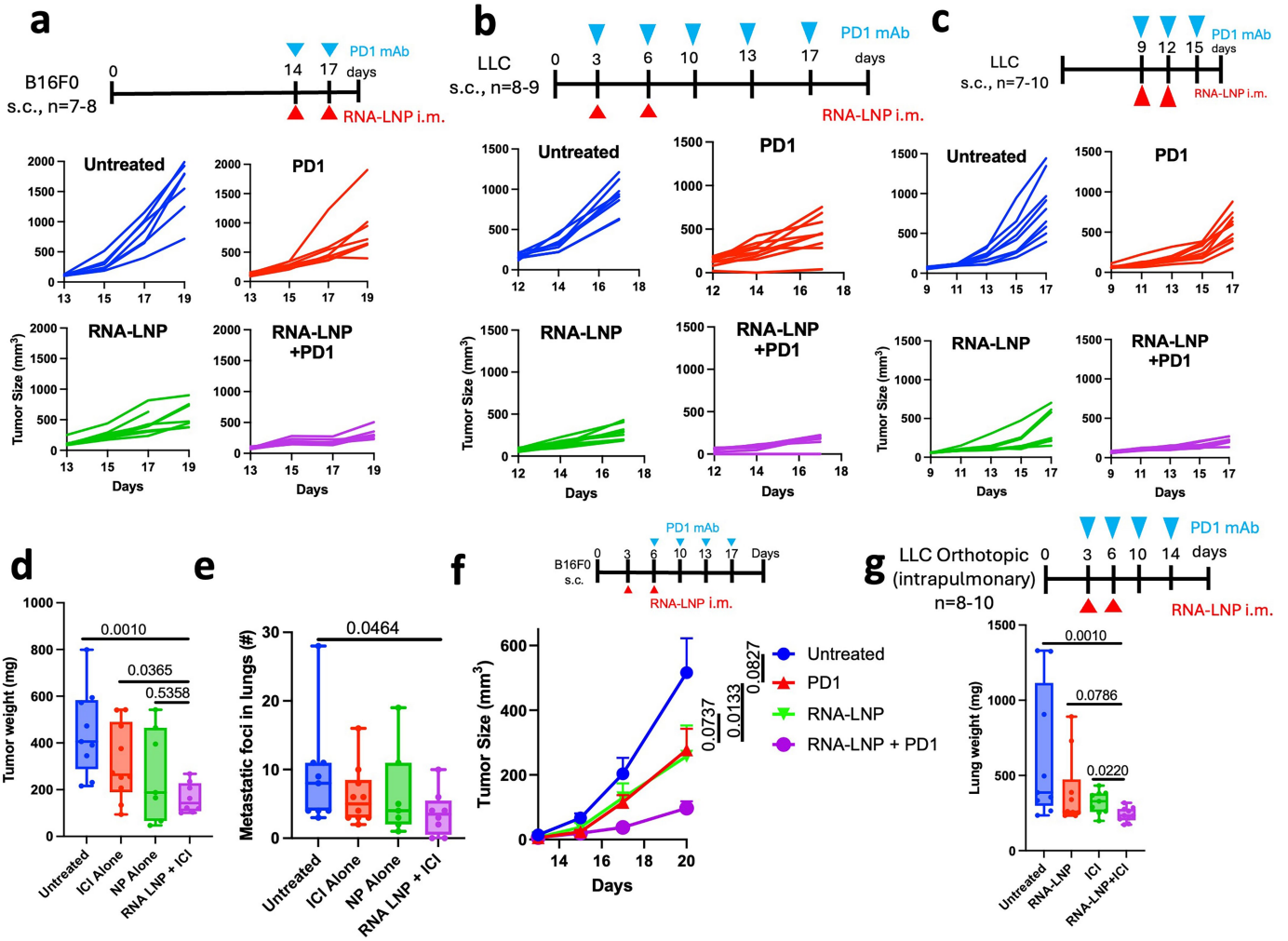

Extended Data Fig. 5 | Spike RNA-LNPs prime anti-cancer immunity in preclinical models. a, Graphical experimental design and individual tumour growth curves of C57Bl6 mice inoculated with B16F0 (50,000 cells) and vaccinated with RNA-LNP i.m. (Day 14,17) with and without anti-PD1. In this experiment, groups included untreated (n = 7), PD1 mAb alone (n = 8), RNA-LNP alone (n = 8), and RNA-LNP and anti-PD1 mAb (n = 8). **b**, Graphical experimental design and individual tumour growth curves for C57Bl/6 mice inoculated with LLC (200,000 cells) and vaccinated with spike RNA-LNP (Day 3,6) with and without anti-PD1 mAbs. In this experiment, groups included untreated (n = 8), anti-PD1 mAb alone (n = 9), RNA-LNP alone (n = 9), and RNA-LNP and anti-PD1 mAb (n = 9). **c**, Graphical experimental design of individual tumour growth curves (**c**), boxplots of tumours weights (**d**) and counts of metastatic tumours in lungs on Day 17 (**e**) in C57Bl/6 mice inoculated with LLC (200,000 cells) and vaccinated with spike RNA-LNP i.m. (Day 9,12) with and without anti-PD1. In this experiment, groups included untreated (n = 9), anti-PD1 mAb alone (n = 10), RNA-LNP alone (n = 7), and RNA-LNP and anti-PD1 mAb (n = 7). **f**, Tumour growth for C57Bl6 mice inoculated with B16F0 (50,000 cells) and vaccinated with RNA-LNP i.m. (Day 3, 6) with and without anti-PD1 (Day 6, 10, 13, 17) (n = 9). **g**, Lung weight in orthotopic LLC tumours (100,000 cells) treated with RNA-LNPs (Days 3 and 6) with or without anti-PD1. In this experiment, groups included untreated (n = 9), anti-PD1 mAb alone (n = 10), RNA-LNP alone (n = 9), and RNA-LNP and anti-PD1 mAb (n = 10). Significance was determined by two-tailed Mann-Whitney U test (**d, e, g**) and two-way ANOVA/mixed-effect analysis with Geisser-greenhouse correction (**f**). All p values are two-tailed. For **d-e** and **g**, whiskers extend to highest and lowest values from a box drawn between 1st and 3rd quartiles with a line centred at the median. **f**, data are represented as mean +/- SEM.

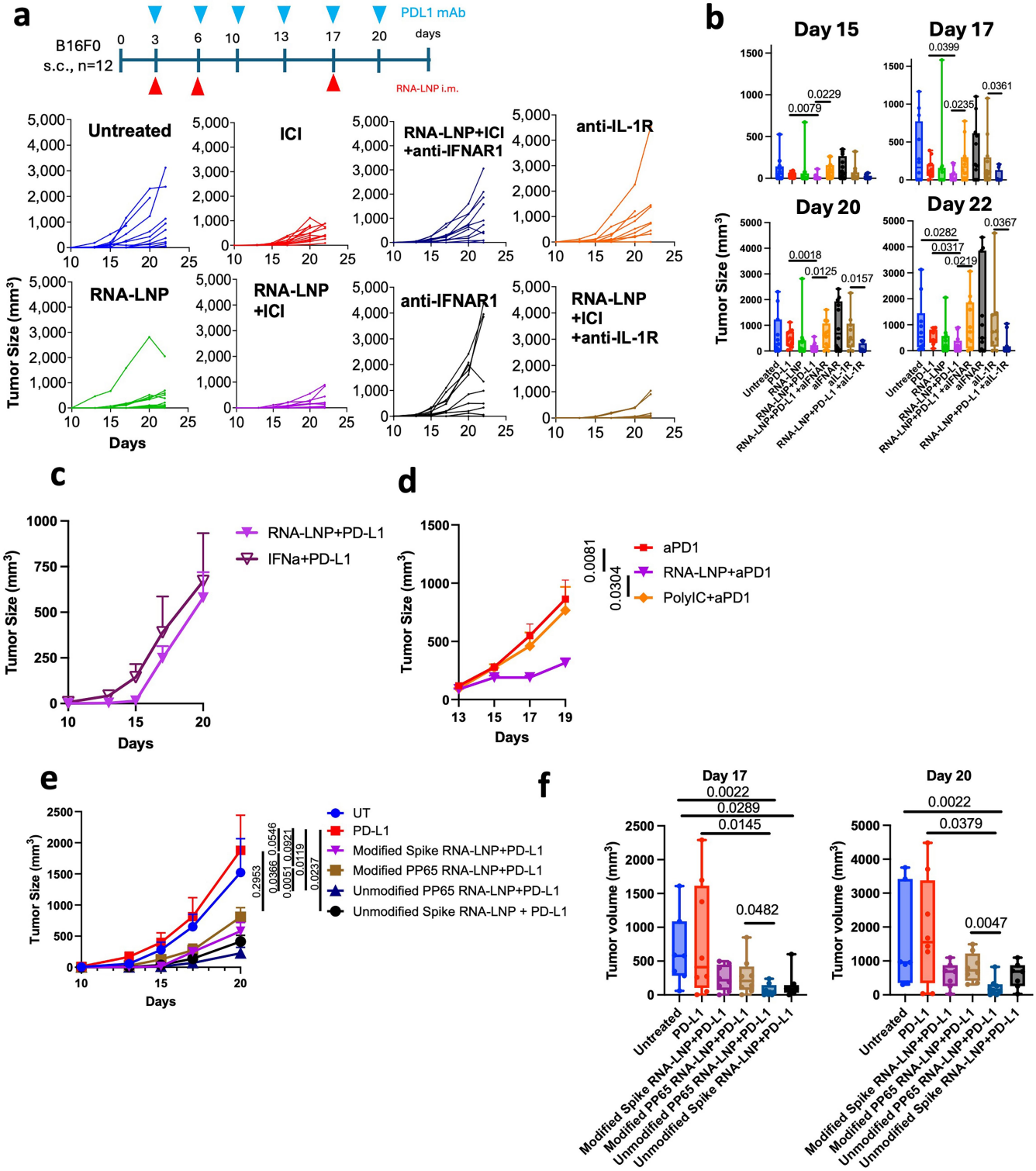

Extended Data Fig. 6 | Antitumor effects of RNA-LNPs are mediated by Type I IFN. a, b, Graphical experimental design, individual tumour growth curves (**a**) and tumour volume (**b**) for C57Bl6 mice inoculated with B16F0 (50,000 cells) and vaccinated with RNA-LNPs (Day 3, 6, 20) with and without anti-PD-L1 and anti-IFNAR1 or anti-IL-1R mAbs (n = 12/group). **c**, Tumour growth for C57Bl/6 mice with subcutaneous B16F0 tumours (50,000 cells) treated with anti-PD-L1 and either RNA-LNPs or exogenous IFN-α (Days 3, 6, and 20) (n = 8/group). Early differences in tumour growth volumes were lost by day 20 without continued treatment. **d**, C57Bl/6 mice with s.c. B16F0 tumours (50,000 cells) are treated with anti-PD1 starting on Day 14/17/20 with or without RNA-LNPs or Poly I:C (Days 14,17) (n = 8/group). **e**, Tumour growth for C57Bl/6 mice with B16F0 tumours (50,000 cells) treated with anti-PD-L1(Days 3/6/10/13/17/20) with or without RNA-LNPs (Days 3,6,20) containing mRNA coding for the Spike or the CMV antigen pp65 incorporating N1-methyl pseudouridine ("modified") or wild-type uridine ("unmodified") and **(f)** boxplots of day 17 and day 20 tumour volumes (n = 8/group). Tumour measurements from mice that met humane end points prior to each measurement day are excluded (Day 17: n = 1 (Untreated), Day 20: n = 2 (Untreated (n = 1) and Modified Spike RNA-LNP + PD-L1 (n = 1)) (see data file). Significance was determined by two-tailed Mann-Whitney U test (**b,f**) and two-way ANOVA/mixed-effect analysis with Geisser-Greenhouse correction (**c,d,e**). Data are displayed as means with standard error. Boxplots in **b** and **f** display whiskers extending to the highest and lowest values from a box drawn between the 1st and 3rd quartiles with a line centred at the median. For **c-e**, data are represented as mean +/- SEM.

a

Sample ID	Intensity	Background intensity	Corrected intensity	Detected dsRNA (%)
Blank	1,232,790	1,701	1,231,089	0.000
Spike RNA	6,527,004	1,918	6,525,086	0.011
Spike ssRNA	2,075,198	1,812	2,073,386	-0.002

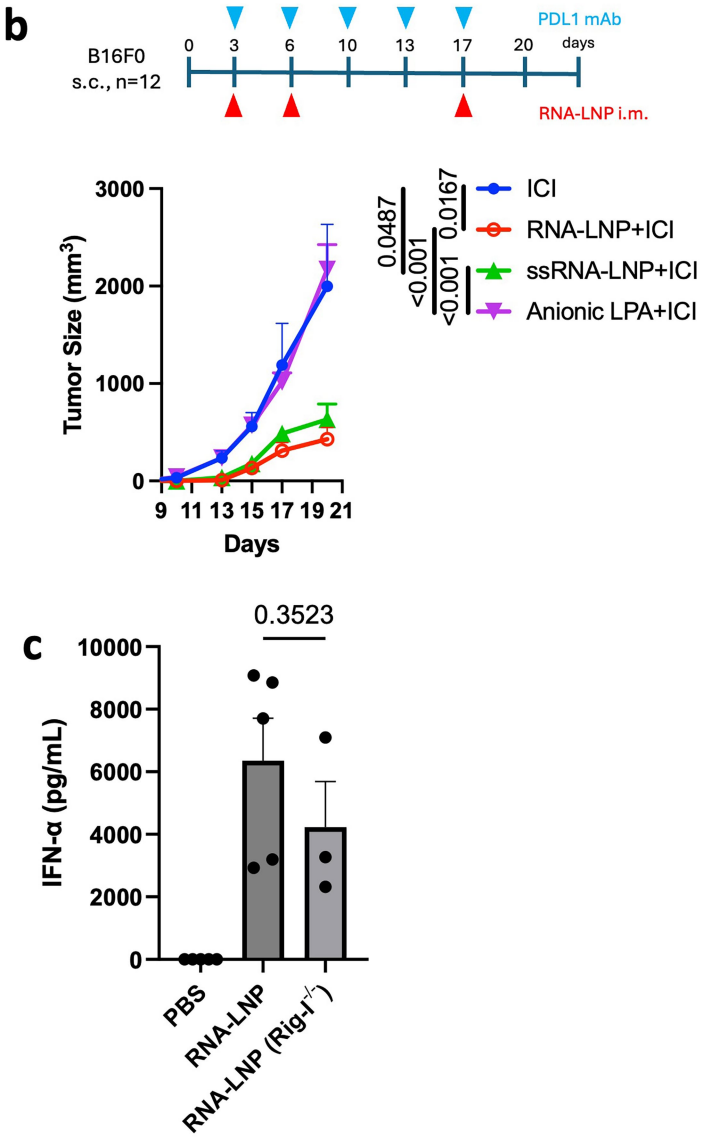

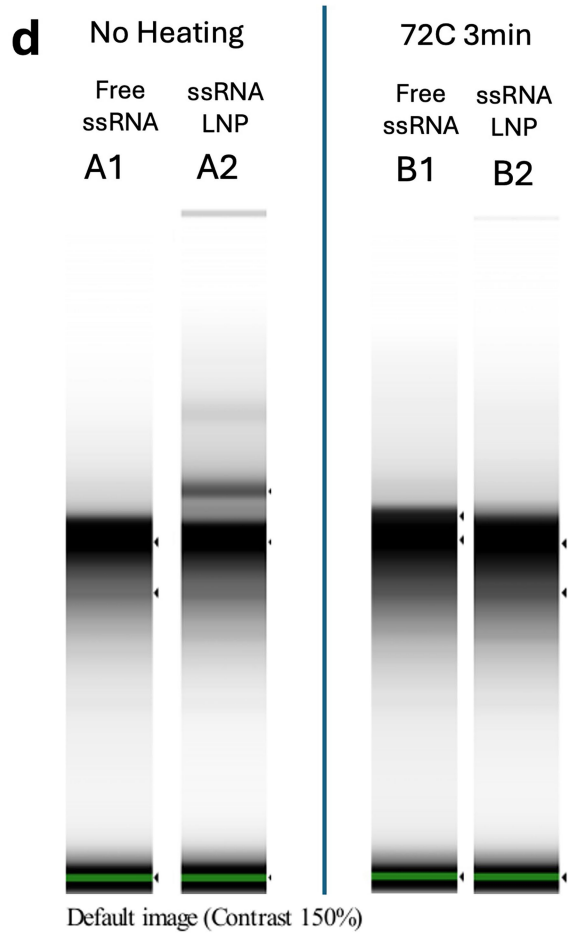

Extended Data Fig. 7 | ssRNA RNA extracted from RNA-LNPs contains high molecular weight secondary structures. a, QC analysis of dsRNA contamination before and after purification (analysis performed by Genscript's dsRNA residue assay). **b**, Tumour growth for mice with B16F0 tumours (50,000 cells) treated with anti-PDL1 mAbs with or without RNA-LNPs versus anionic (LPA) versus ssRNA (Days 3,6, 17) (n = 12). In this experiment, anionic LPA was synthesized by mixing DOTAP liposomes with mRNA at a 1:1 mass to mass ratio to formulate lipid particle aggregates (see methods). **c**, ELISA for IFN-α in serum collected from wildtype C57Bl/6 mice (n = 5) 24 h after treatment with PBS (WT PBS) or RNA-LNP (WT RNA-LNP), or RIG-I null mice (n = 3) treated with RNA-LNP (RIG-I -/- RNA-LNP). **d**, Non-complexed RNA (A1, B1) and LNP extracted RNA (A2,B2) analysed on a tape station with or without heating. Data are displayed as means with standard error. Significance was determined by two-way ANOVA/mixed-effect analysis with Geisser-greenhouse correction (**b**), and two-tailed unpaired t tests (**c**). For **b**, data are represented as mean +/- SEM. For **c**, the height of the bars represents mean and error bars represent +SEM.

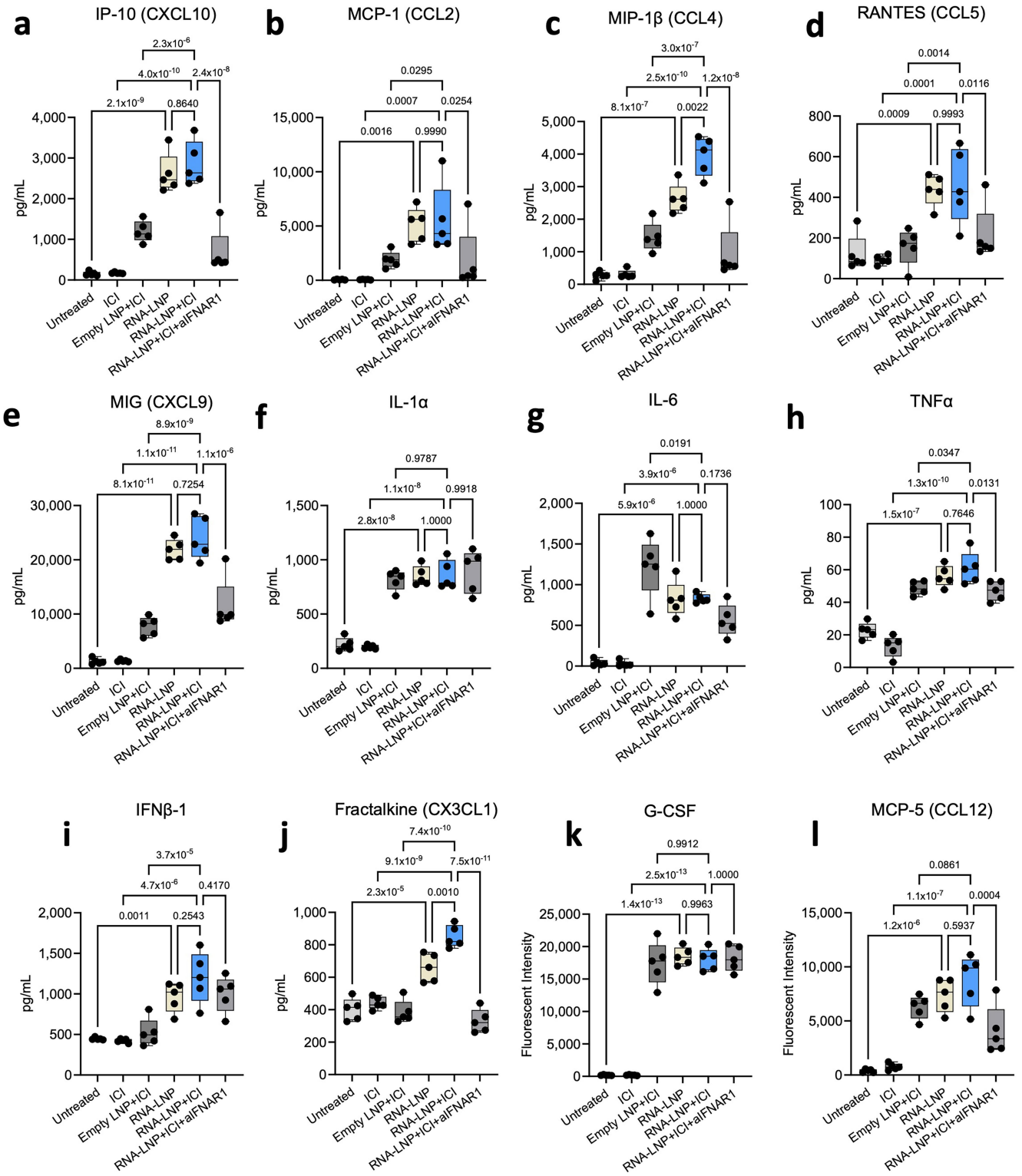

Extended Data Fig. 8 | RNA-LNPs elicit a dramatic shift in systemic cytokines/chemokines. a-l, Cytokine/chemokine multiplex panel. Values are represented as pg/mL (**a-j**) for samples within the standard curve, and as fluorescent intensity values for cytokines above the standard curve (**k-l**). Plasma from subcutaneous B16F0 (50,000 cells) bearing C57Bl/6 animals (n = 5/group) 24 h after one RNA-LNP vaccine i.m. Whiskers extend to highest and lowest values, with a box shown between 1st and 3rd quartiles with a line centred at median. Significance was determined by one-way ANOVA analysis followed by two-tailed Šidák correction.

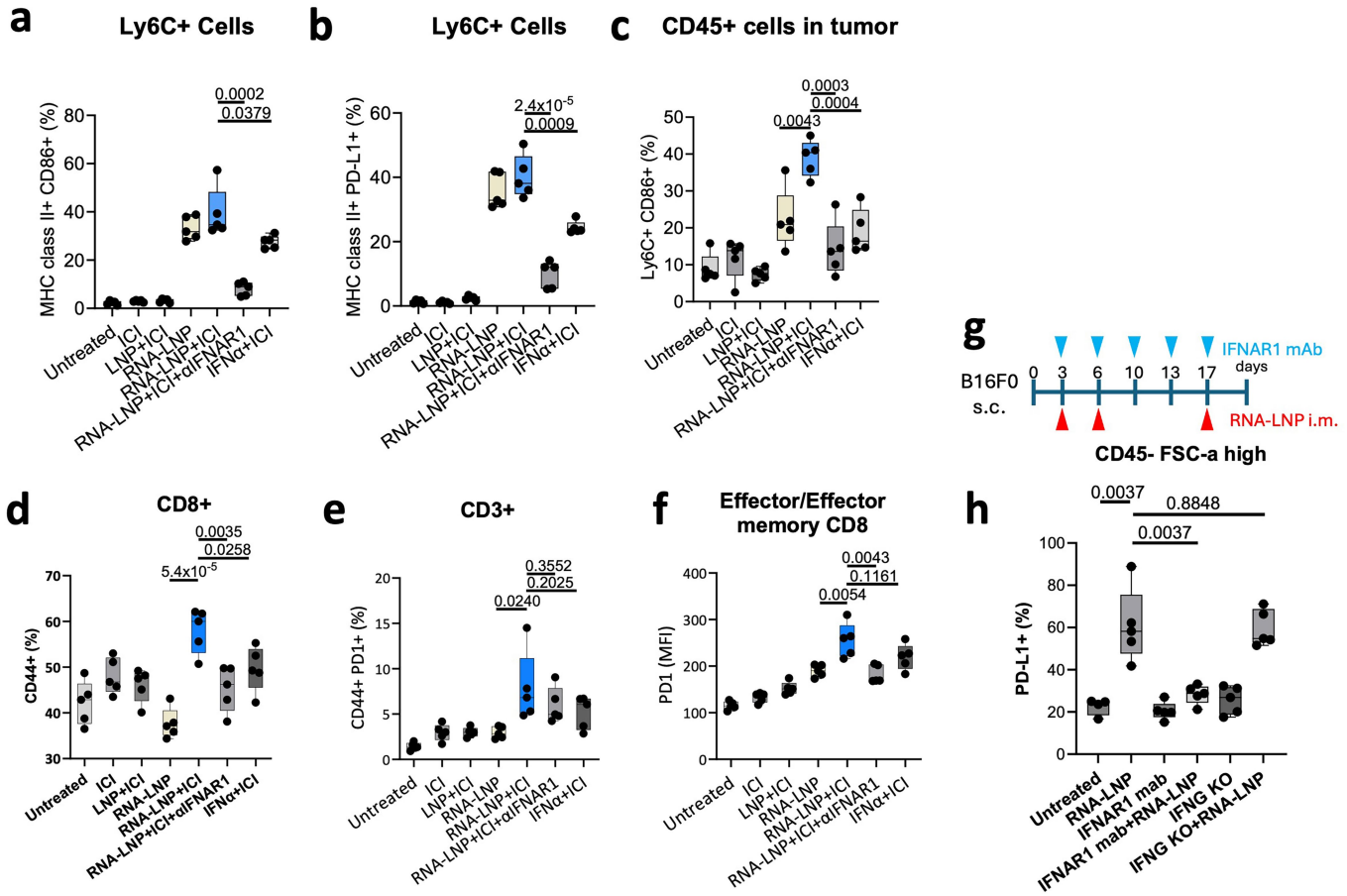

Extended Data Fig. 9 | Spike RNA-LNP prime anti-cancer immunity in an IFN-I dependent manner. a-b, Box-Plots of cellular phenotyping within 24 h of 3rd RNA-LNP vaccine i.m. (Days 3, 6, 20) from spleens of C57Bl/6 animals bearing subcutaneous B16F0 (50,000 cells, n = 5/group). **a**, Percentage of activated (MHCII + CD86 +) Ly6C+ cells. **b**, MHCII and PD-L1 positive of Ly6C+ cells (%). **c**, Prevalence of CD86 + Ly6C+ cells of CD45+ cells in tumours. **d-f**, Box-plots of cellular phenotyping within 24 h of 3rd RNA-LNP vaccine i.m. (Days 3, 6, 20) from spleens of subcutaneous B16F0 (50,000 cells) bearing C57Bl/6 animals (n = 5/group) for (**d**) percentage of CD44 + T cells in the CD8+ compartment, (**e**) percentage of CD44+PD1+ among CD3+ cells, and (**f**) median fluorescence intensity (MFI) of PD1 on effector CD8 T cells. **g,h**. Upregulation of PDL1 on tumour cells is dependent on Type I IFN. Wild type and IFN-gamma KO mice with s.c. B16F0 tumours (50,000 cells) were treated with three doses of mRNA vaccines (Days 3, 6, and 17) with or without twice weekly antibodies blocking the IFN-a receptor (IFNAR1) (n = 4 untreated, n = 5 for all other groups). PDL1 expression on tumour cells was evaluated on Day 18 with flow cytometry. Whiskers extend to highest and lowest values from a box drawn between 1st and 3rd quartiles with a line centred at median. Significance was determined using two-tailed unpaired t tests.

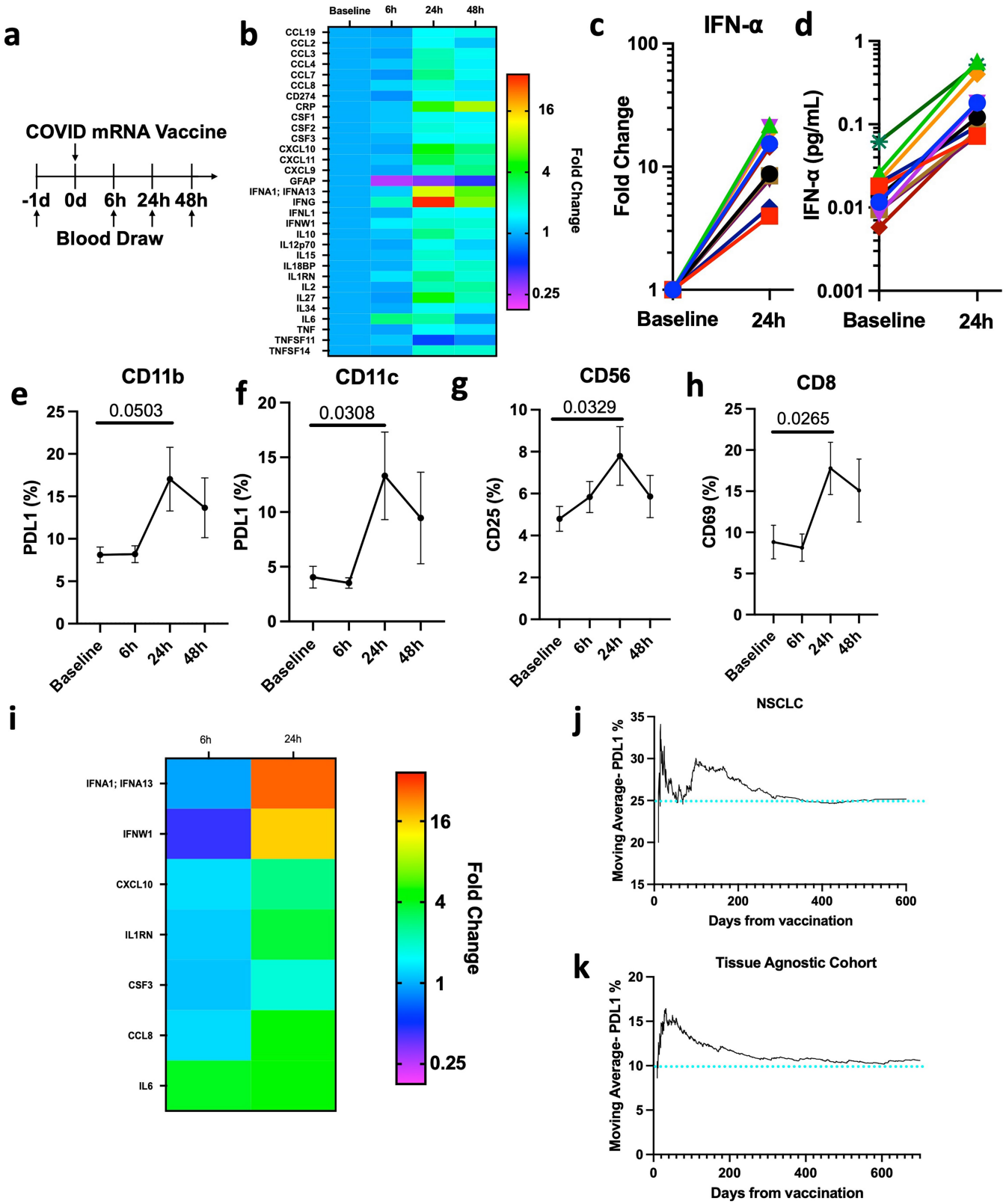

Extended Data Fig. 10 | See next page for caption.

Extended Data Fig. 10 | COVID mRNA vaccines generate a surge in IFN-α, innate immune activation and adaptive immunity in humans. a, Schematic depicting the experimental design wherein blood was drawn from eleven healthy subjects at baseline and 6 h, 24 h, and 48 h after BNT162b COVID mRNA immunization. **b**, Heat map displaying dynamic expression of the cytokines that are significantly elevated at 24 h at the following time points: 6 h, 24 h, and 48 h after COVID mRNA vaccination. Significant variables were defined as those with p < .05 and log2-Fold-Change with absolute value greater than 0.5 following linear modelling with fixed effect. Adjusted p values were calculated using moderated two-tailed t-tests with FDR correction for multiple testing. **c**-**d**, Individual data points highlighting changes in expression of IFN-α from baseline to 24 h for healthy volunteers (n = 11) expressed as fold change from baseline (**c**) and concentration (**d**). **e**-**h**, PD-L1 expression on circulating myeloid cells (**e**) and dendritic cells (**f**), activation of NK cells (**g**), and activation of T cells expressed at percentage of CD69 + CD8+ cells (**h**) at baseline, 6 h (6 h), 24 h (24 h), and 48 h (48 h) after immunization (n = 7). Data are presented as means with standard error. p values in **e**-**h** are results of two-tailed paired t tests. **i**, Heatmap displaying differentially expressed cytokines for patients receiving Spikevax (2023-2024 formulation, 50 µg mRNA) relative to the Comirnaty COVID mRNA vaccine (2024-2025 formulation, 30 µg mRNA). Moderated t tests were performed on per-patient $\log_2$ fold change differences between cytokines at baseline vs 6 h or 24 h, with direct comparison of fold change from baseline in volunteers treated with either Moderna or Pfizer at each timepoint. Relative fold change for Moderna compared to Pfizer was displayed for differences that were significant with $|\log_2 FC| > 0.5$ and $p < 0.05$ at either 6 h or 24 h after multiple comparisons testing. **j**,**k**. Cumulative moving average of PDL1 expression for patients in the NSCLC (**j**) and Tissue Agnostic (**k**) cohorts stratified by the time from each patient's most recent COVID mRNA vaccine. Data indicates the average of all TPS measurements from patients who received biopsy within each period from COVID mRNA immunization. Blue lines indicate unvaccinated patient average TPS.

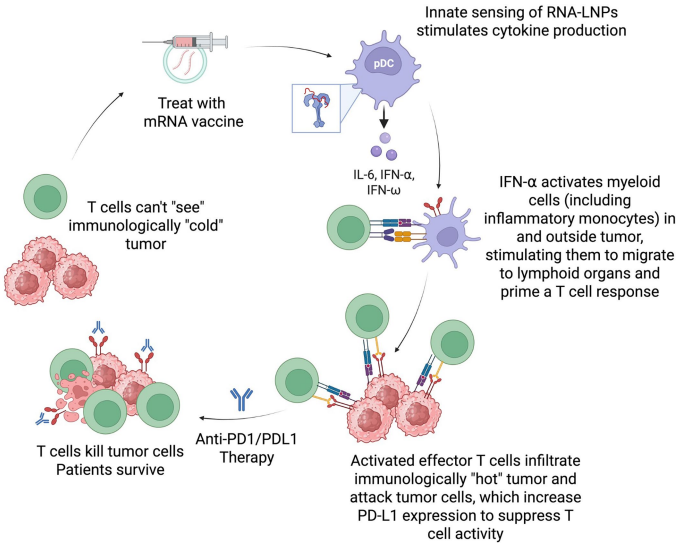

Extended Data Fig. 11 | Schematic describing how mRNA vaccines sensitize immunologically "cold" tumours. RNA-LNPs stimulate production of IFN-α, leading APCs to prime T cells in lymphoid organs. These primed, tumour-reactive T cells then infiltrate tumours and begin killing tumour cells. Tumour cells respond by expressing PD-L1. Combination therapy with RNA-LNPs and ICIs overcomes this resistance mechanism, leading to tumour rejection. Image created in BioRender (Grippin, A. (2025) https://BioRender.com/zcaaisj).

nature portfolio

Corresponding author(s): Steven Lin, MD, PhD
Elias Sayour, MD, PhD
Adam Grippin, MD, PhD

Last updated by author(s): October 20, 2025

Reporting Summary

Nature Portfolio wishes to improve the reproducibility of the work that we publish. This form provides structure for consistency and transparency in reporting. For further information on Nature Portfolio policies, see our Editorial Policies and the Editorial Policy Checklist.

Please do not complete any field with "not applicable" or n/a. Refer to the help text for what text to use if an item is not relevant to your study.
For final submission: please carefully check your responses for accuracy; you will not be able to make changes later.

Statistics

For all statistical analyses, confirm that the following items are present in the figure legend, table legend, main text, or Methods section.

n/a	Confirmed	
☐	☒	The exact sample size (*n*) for each experimental group/condition, given as a discrete number and unit of measurement
☐	☒	A statement on whether measurements were taken from distinct samples or whether the same sample was measured repeatedly
☐	☒	The statistical test(s) used AND whether they are one- or two-sided *Only common tests should be described solely by name; describe more complex techniques in the Methods section.*
☐	☒	A description of all covariates tested
☐	☒	A description of any assumptions or corrections, such as tests of normality and adjustment for multiple comparisons
☐	☒	A full description of the statistical parameters including central tendency (e.g. means) or other basic estimates (e.g. regression coefficient) AND variation (e.g. standard deviation) or associated estimates of uncertainty (e.g. confidence intervals)
☐	☒	For null hypothesis testing, the test statistic (e.g. *F*, *t*, *r*) with confidence intervals, effect sizes, degrees of freedom and *P* value noted *Give P values as exact values whenever suitable.*
☒	☐	For Bayesian analysis, information on the choice of priors and Markov chain Monte Carlo settings
☒	☐	For hierarchical and complex designs, identification of the appropriate level for tests and full reporting of outcomes
☐	☒	Estimates of effect sizes (e.g. Cohen's *d*, Pearson's *r*), indicating how they were calculated

Our web collection on statistics for biologists contains articles on many of the points above.

Software and code

Policy information about availability of computer code

Data collection

- All experimental data was collected and stored according to The University of Texas MD Anderson Cancer Center intellectual property protection policy.
- Clinical data was obtained from review of electronic medical records.
- Human flow cytometry data was acquired on Aurora Spectral Flow Cytometer (Cytek) and murine flow cytometry data was acquired on Symphony A3 (BD Biosciences). Both were analyzed using FlowJo 10.8.1 software (BD Biosciences).
- Particle characteristics were collected using Malvern Panalytical's Zetasizer Ultra and NanoSight's NS300 nanoparticle tracking analysis.

Data analysis

Analysis was performed using standard protocols. No custom code was used for this study. Statistics were completed with R version 4.4.2 (2024-10-31) and GraphPad Prism v10.3 and v10.6. Flow cytometry data was analyzed with FlowJo 10.8.1 and FlowJo 10.10.0 (BD Biosciences). St.dev. were exported from ZS Xplorer.

For manuscripts utilizing custom algorithms or software that are central to the research but not yet described in published literature, software must be made available to editors and reviewers. We strongly encourage code deposition in a community repository (e.g. GitHub). See the Nature Portfolio guidelines for submitting code & software for further information.

Data

Policy information about availability of data

All manuscripts must include a data availability statement. This statement should provide the following information, where applicable:

- Accession codes, unique identifiers, or web links for publicly available datasets
- A description of any restrictions on data availability
- For clinical datasets or third party data, please ensure that the statement adheres to our policy

Data generated in this study are available in the article and its supplementary files. Source data are also provided with this paper. All clinical data is de-identified to protect patient privacy.

Research involving human participants, their data, or biological material

Policy information about studies with human participants or human data. See also policy information about sex, gender (identity/presentation), and sexual orientation and race, ethnicity and racism.

Reporting on sex and gender	Clinical data was collected retrospectively for all patients for whom data was available at our institution. Patients' self identified gender is presented as recorded in the electronic medical record.
Reporting on race, ethnicity, or other socially relevant groupings	Self-identified ethnicity (Caucasian, black, asian, hispanic/latino) was reported as recorded in the electronic medical record.
Population characteristics	University of Texas MD Anderson Cancer Center institutional review board approval was obtained. Healthy volunteers (>18yo) were recruited and provided informed consent for serum and blood analysis. Chart review for this study included three groups of patients: (a) patients with biopsy confirmed Stage III or Stage IV non-small cell lung cancer (NSCLC) between 1/2017 and 9/2022, (b) patients with melanoma treated with immune checkpoint blockade between 1/2019 and 12/2022, and (c) patients with any tumor histology with pathology results for PD-L1 from January 2020 to October 2023. Informed consent was waived due to the retrospective and de-identified nature of the data. The data collection cutoff was 9/1/2024; data analysis was performed from 9/1/2024 to 7/29/2025. Patient populations are described in detail in the manuscript and supplemental materials.
Recruitment	Healthy volunteers working in the Texas Medical Center and planning to obtain a COVID mRNA vaccine were recruited for the biomarker portion of this study. This group may be more likely to receive routine vaccinations compared to the general population.
Ethics oversight	This study was approved by the University of Texas MD Anderson Institutional Review Board.

Note that full information on the approval of the study protocol must also be provided in the manuscript.

Field-specific reporting

Please select the one below that is the best fit for your research. If you are not sure, read the appropriate sections before making your selection.

☒ Life sciences ☐ Behavioural & social sciences ☐ Ecological, evolutionary & environmental sciences

For a reference copy of the document with all sections, see nature.com/documents/nr-reporting-summary-flat.pdf

Life sciences study design

All studies must disclose on these points even when the disclosure is negative.

Sample size	Retrospective clinical data included all available data points. Animal studies were completed with samples sizes based on previous studies from our group evaluating anti-tumor efficacy according to the University of Florida and University of Texas MD Anderson Cancer Center IACUC protocols.
Data exclusions	No data was excluded.
Replication	All clinical findings were replicated in at least two patient populations. Translational data presented in the manuscript included experiments performed in two independent laboratories. Major findings were validated in multiple tumor models. All attempts at replication were successful.
Randomization	Mice were randomly allocated to treatment arms described in each experiment once they reached the pre-determined tumor volume and/or designated time post tumor injection.
Blinding	Investigators were blinded to groups for tumor measurements but were not blinded during data analysis.

Reporting for specific materials, systems and methods

We require information from authors about some types of materials, experimental systems and methods used in many studies. Here, indicate whether each material, system or method listed is relevant to your study. If you are not sure if a list item applies to your research, read the appropriate section before selecting a response.

Materials & experimental systems

n/a	Involved in the study
☐	☒ Antibodies
☐	☒ Eukaryotic cell lines
☒	☐ Palaeontology and archaeology
☐	☒ Animals and other organisms
☐	☒ Clinical data
☒	☐ Dual use research of concern
☒	☐ Plants

Methods

n/a	Involved in the study
☒	☐ ChIP-seq
☐	☒ Flow cytometry
☒	☐ MRI-based neuroimaging

Antibodies

Antibodies used

The following antibodies were used for human samples:

Anti-CD14 (clone 63D3, BioLegend, catalog #367156); Anti-PD-1 (clone EH12.2H7, BioLegend, catalog #329920); Human TruStain FcX™ (BioLegend, catalog #422302); Anti-CD25 (clone BC96, BioLegend, catalog #302612); Anti-CD19 (clone HIB19, BioLegend, catalog #302274); Anti-CD8 (clone SK1, BioLegend, catalog #344766); Anti-PD-L1 (clone 29E.2A3, BioLegend, catalog #329738); Anti-CD16 (clone 3G8, BD Biosciences, catalog #612944); Anti-CD11c (clone B-ly6, BD Biosciences, catalog #741358); Anti-CD11b (clone M1/70, BD Biosciences, catalog #612977); Anti-CCR7 (CD197) (clone 3D12, BD Biosciences, catalog #741786); Anti-CD15 (clone 7C3.RMAB, BD Biosciences, catalog #568935); Anti-CD4 (clone L200, BD Biosciences, catalog #566148); Anti-HLA-DR (clone G46-6, BD Biosciences, catalog #563083); Anti-GITR (CD357) (clone V27-580, BD Biosciences, catalog #747664); Anti-CD127 (IL-7Rα) (clone hIL-7R-M21, BD Biosciences, catalog #563225); Anti-CD56 (clone NCAM16.2, BD Biosciences, catalog #563169); Anti-CD80 (clone L307.4, BD Biosciences, catalog #564159); Anti-Granzyme A (clone CB9, BD Biosciences, catalog #568661); Anti-Granzyme B (clone GB11, BD Biosciences, catalog #571117); Anti-CD86 (B7-2) (clone 2331 (FUN-1), BD Biosciences, catalog #755689); Anti-CD178 (FasL) (clone NOK-1, BD Biosciences, catalog #564261); Anti-CD33 (clone HIM3-4, BD Biosciences, catalog #758223); Anti-CD68 (clone Y1/82A, BD Biosciences, catalog #562111); Anti-CD45 (clone HI30, BD Biosciences, catalog #566961); Anti-CD3 (clone SK7, BD Biosciences, catalog #560176); Brilliant Stain Buffer Plus (BD Biosciences, catalog #566385); Anti-CD45RA (clone HI100, BD Biosciences, catalog #568712); Anti-CD69 (clone FN50, BD Biosciences, catalog #751501); Anti- PD-L1 (Clone MIH1, BD Biosciences, catalog #757550);

The following antibodies were used for preclinical experiments:

T Cell Panel:
Anti-CD3 (clone 17A2, BD, catalog #740268); Anti-CD161 (clone PK136, BD, catalog #741233); Anti-CD127 (clone SB/199, BD, catalog #612841); Anti-CD4 (clone GK1.5, BioLegend, catalog #100428); Anti-PD1 (clone J43, BD, catalog #563059); Anti-CD25 (clone PC61, BioLegend, catalog #102051); Anti-CD44 (clone IM7, BioLegend, catalog #103016); Anti-KLRG1 (clone 2F1, BD, catalog #758385); Anti-CD69 (clone H1.2F3, BD, catalog #756896); Anti-CD62L (clone MEL-14, BD, catalog #569209); Anti-LAG-3 (clone C9B7W, BD, catalog #552380); Anti-TIM-3 (clone B8.2C12, BioLegend, catalog #134008); Anti-CD8A (clone 53-6.7, BD, catalog #557959); Live/Dead (Thermo, catalog #L10119)

Myeloid Panel:

Anti-CD45 (clone 30-F11, BD, catalog #564279); Anti-CD11c (clone N418, BD, catalog #750450); Anti-CD11c (clone N418, BD, catalog #570292); Anti-CD80 (clone 16-10A1, BD, catalog #612773); Anti-MHC-II (clone M5/114.15.2, BioLegend, catalog #107620); Anti-Ly6G (clone 1A8, BioLegend, catalog #127629); Anti-CD163 (clone S15049I, BioLegend, catalog #155325); Anti-Ly6C (clone HK1.4, BioLegend, catalog #128041); Anti- CD206 (clone C068C2, BioLegend, catalog #141710); Anti-CD86 (clone B7-2, BD, catalog #759079); Anti-F4/80 (clone T45-2342, BD, catalog #569223); Anti-CD11B (clone M1/70, BD, catalog #571473); Anti-PD-L1 (clone 485, Thermo, catalog #MA5-46763); Live/Dead (Thermo, catalog #L10119).

AIM Assay:

Anti-CD40L (clone SA047C3, BD, catalog #157006); Anti-CD25 (clone PC61, BioLegend, catalog #101920); Anti-CD69 (clone H1.2F3, BD, catalog #104514); Anti-CD3 (clone 17A2, BD, catalog #100216); Anti-CD8A (clone 53-6.7, BD, catalog #560182); Anti-CD4 (clone RM4-4, BioLegend, catalog #116008); Anti-4-1BB (clone 17B5, BioLegend, catalog #106106).

Immunofluorescence experiments were completed with the following antibodies:

Anti-CD274 (PD-L1) (clone 2B11D11, Proteintech, catalog #66248-1-Ig, dilution 1:100); Anti-SOX10 (clone SP267, Abcam, catalog #ab227680, dilution 1:200); Anti-CD3 (clone 145 2C11, BD, catalog #553057, dilution 1:100); Anti-CD8 (polyclonal, Invitrogen, catalog #PA5-81344, dilution 1:1000); Anti-PD1 (clone J121, eBioscience, catalog #14-2798-82, dilution 1:100); Goat anti-mouse AF488 (polyclonal, Invitrogen, catalog #A11001, dilution 1:1000); Goat anti-rabbit AF564 (polyclonal, Invitrogen, catalog #A11012, dilution 1:1000); Goat anti-hamster AF647 (polyclonal, Invitrogen, catalog #A78967, dilution 1:1000).

Validation	Validation was completed according to manufacturer recommendations, and prior publications. Antibodies were titrated to identify the concentration with the highest stain index in the cell population of interest

Eukaryotic cell lines

Policy information about cell lines and Sex and Gender in Research

Cell line source(s)	B16F0 and LLC cells were obtained from ATCC.
Authentication	No independent cell authentication was completed by our lab.
Mycoplasma contamination	Mycoplasma testing was performed routinely and cells were not contaminated with mycoplasma.
Commonly misidentified lines (See ICLAC register)	None

Animals and other research organisms

Policy information about studies involving animals; ARRIVE guidelines recommended for reporting animal research, and Sex and Gender in Research

Laboratory animals	4-9 week old C57Bl6 and RIGI-/- mice
Wild animals	No wild animals were used.
Reporting on sex	Sex was not evaluated as an independent variable in this study. Self-reported patient gender is included in the supplement.
Field-collected samples	This study did not include field-collected samples.
Ethics oversight	All experiments in this study were approved by the IACUC at MD Anderson and the University of Florida

Note that full information on the approval of the study protocol must also be provided in the manuscript.

Clinical data

Policy information about clinical studies

All manuscripts should comply with the ICMJE guidelines for publication of clinical research and a completed CONSORT checklist must be included with all submissions.

Clinical trial registration	N/A
Study protocol	Study analysis was retrospective
Data collection	The data collection cutoff was 9/1/2024; data analysis and retrospective chart review were performed from 5/1/2024 to 9/1/2024.
Outcomes	For patients who received COVID-19 mRNA vaccination in both the NSCLC and melanoma datasets, overall survival was calculated as the time between the date of immunotherapy start closest to mRNA vaccination date, and the last follow-up date (for patients who are living) or date of death. For patients who did not receive COVID-19 mRNA vaccination, overall survival was calculated as the time between the initiation of their first ICI start and the date of death or last follow-up. For patients who received COVID mRNA vaccination in both datasets, progression-free survival was calculated as the time between the initiation of ICI closest to mRNA vaccination and the first incidence of either pathology-confirmed recurrence or imaging-confirmed progression, whichever occurred earlier, that was declared progression in their primary medical oncologist's clinical notes. For patients who did not receive COVID mRNA vaccination, progression-free survival was calculated as the time between their first ICI start date and clinician-confirmed progression as described in the text.

Plants

Seed stocks	N/A
Novel plant genotypes	N/A
Authentication	N/A

Flow Cytometry

Plots

Confirm that:

☒ The axis labels state the marker and fluorochrome used (e.g. CD4-FITC).

☒ The axis scales are clearly visible. Include numbers along axes only for bottom left plot of group (a 'group' is an analysis of identical markers).

☒ All plots are contour plots with outliers or pseudocolor plots.

☒ A numerical value for number of cells or percentage (with statistics) is provided.

Methodology

Sample preparation	For human samples, PBMCs were thawed in a 37°C water bath and immediately transferred into a 50 mL tube containing 9 mL of complete RPMI media (RPMI + 10% FBS) in a ratio of 1 part cells to 9 parts media. Cells were centrifuged at 400g for 10 minutes, and the supernatant was decanted. The cell pellet was resuspended in 1 mL of PBS, and incubated with live/dead marker (1 µL per 1000 µL of cell suspension, containing 1-10 million cells per mL) for 30 minutes at 4°C. After incubation, 3 mL of PBS + 2% FBS was added, and the cells were centrifuged again at 400g for 8 minutes and the supernatant was decanted. Cells were then pre-incubated with 5 µL of Human TruStain FcX™ (BioLegend, cat. 422302) per 100 µL of cell suspension for 5 minutes at room temperature. The cells were then washed with PBS and centrifuged at 400g for 6 minutes. After decanting the supernatant, 10 µL of Brilliant Buffer was added to each tube, and the mixture was allowed to sit for 5 minutes before addition of antibodies targeting extracellular markers and the cells were incubated for 20 minutes at room temperature in the dark. After incubation, the cells were washed and fixed in the dark for 45 minutes at 4°C with 500 µL of Fixation solution (BD). Cells were then permeabilized with 2 mL permeabilization buffer. Intracellular stains were added in permeabilization buffer, and the cells were incubated for approximately 40 minutes at room temperature. After incubation, cells were washed with permeabilization buffer and resuspended in 200 µL of PBS + 2% FBS. For murine samples, 1x10^6 cells from tumors or spleen were placed into 96 well v-bottom plates. Unless stated otherwise wash steps were done by centrifugation steps were performed at 500G for 5 minutes at 4C and resuspension of cells with 200uL of buffer with mixing done via pipetting. Cells were washed with cold PBS and stained with 100uL of live/dead stain (Thermo, cat. L10119) for 30 minutes at 4C. Live dead dye was quenched with 100uL of cold PBS and washed one time with cold FACs buffer (PBS with 2% FBS). Cells were centrifuged and resuspended with 10uL True stain FCX buffer (BioLegend, cat. 422302) diluted to 100ug/mL with FACs buffer for 10 minutes. 90uL of antibodies (Antibody table 1 and 2) and Brilliant Stain buffer (BD, cat. 563794) were added and incubated for 30 minutes at 4C. 100uL of FACs buffer was added to each well and washed 2 times with cold FACs buffer. Cells were fixed for 15 minutes with 100uL of Cytofix buffer (BD, cat. 554655) at 4C 100uL of PBS was added to each sample and cells were washed 2 times and stored in FACs buffer at 4C in the dark until analysis. Compensation was performed using Ultracomp eBeads (Thermo Fisher Scientific, cat. 01-2222-42) and ArC amine reactive compensation beads (Thermo Fisher Scientific, cat. A10346)
Instrument	Human samples: Cytek Aurora Spectral Flow Cytometer. Murine samples: BD Symphony A3.
Software	FlowJo v10.10.0
Cell population abundance	Studies were performed on PBMCs (human), splenocytes, (murine) and whole tumors (murine).
Gating strategy	FSC-A/SSC-A gates were used to select mononuclear cells. FSC-A/FSC-H gates were then used to gate single cells. Live cells were identified with a live dead marker. Fluorescence minus one controls were used to identify the postive and negative populations for each additional marker.

☒ Tick this box to confirm that a figure exemplifying the gating strategy is provided in the Supplementary Information.